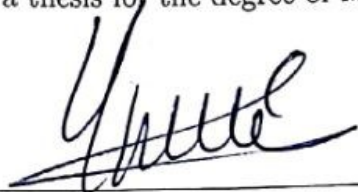# DEVELOPMENT OF A HISTOTRIPSY AGENT USING HOST-GUEST INTERACTION

A THESIS SUBMITTED TO

THE GRADUATE SCHOOL OF

ENGINEERING AND NATURAL SCIENCES

OF ISTANBUL MEDIPOL UNIVERSITY

IN PARTIAL FULFILLMENT OF THE REQUIREMENTS FOR

THE DEGREE OF

MASTER OF SCIENCE

IN

BIOMEDICAL ENGINEERING AND BIOINFORMATICS

By

Tanzeel Ur Rehman

December, 2017

Development of a Histotripsy Agent using Host-Guest Interaction

By Tanzeel Ur Rehman

November, 2017

We certify that we have read this thesis and that in our opinion it is fully adequate, in scope and in quality, as a thesis for the degree of Master of Science.

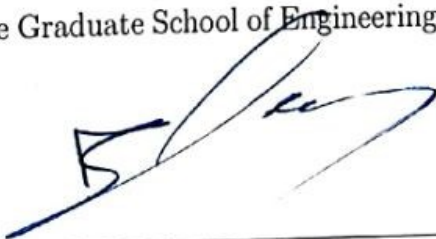Assoc. Prof. Dr. Yasemin Yuksel Durmaz(Advisor)

Asst. Prof. Dr. Mehmet Ucisik

Assoc. Prof. Dr. Bunyamin Karagoz

Approved by the Graduate School of Engineering and Natural Sciences:

Prof. Dr. Talip Alp

Director of the Graduate School of Engineering and Natural Sciences

I hereby declare that all information in this document has been obtained and presented in accordance with academic rules and ethical conduct. I also declare that, as required by these rules and conduct, I have fully cited and referenced all material and results that are not original to this work.

Name, Last Name: TANZEEL UR REHMAN

Signature   :

ABSTRACT

DEVELOPMENT OF A HISTOTRIPSY AGENT USING HOST-GUEST INTERACTION

Tanzeel Ur Rehman

M.S. in Biomedical Engineering and Bioinformatics
Advisor: Assoc. Prof. Dr. Yasemin Yuksel Durmaz
December, 2017

Histotripsy is a mechanical cell ablation technique, which works on the mechanism of acoustic cavitation using microsecond-long, high-frequency ultrasound (US) pulses that can generate a bubble cloud (cavitation) using the already existing gas pockets in the tissue. Once the bubble cloud gains enough energy, it collapses resulting in the cellular destruction/ablation of the surrounding tissue. Histotripsy requires extremely high pressures to initiate cavitation in the tissue. Recently developed Nanodroplet Mediated Histotripsy (NMH) addresses this limitation by lowering the cavitation threshold using perfluorocarbon filled nanodroplets as a histotripsy agent. Despite the fact that these nanodroplets work perfectly for NMH, the synthesis of these nanodroplets is complex, and requires expertise in the field of polymer chemistry. Thus, this work aims to address the need for a new histotripsy agent that can work as effectively as nanodroplets, but have better potential in terms of being more user-friendly, straightforward, and economical. Two currently available Food and Drug Administration (FDA) approved and commercial compounds, β-cyclodextrin (BCD) and perfluorohexane (PFH), were used to obtain an inclusion complex (IC) through host-guest interaction, where hydrophobic cavity of BCD accommodates hydrophobic perflurorcarbon that might act as cavitation nuclei, and lower the threshold during histotripsy treatment.

PFH was successfully encapsulated in the cavity of BCD with an encapsulation efficiency of 98%. Physiochemical characterization of the IC supported the complex formation, and indicated the potential of having more than one PFC in the cavity, depending on PFH/BCD ratio. The size of the complex was measured at 48 nm, which is smaller than the size of nanodroplets. However, it has a tendency to form a bigger self-assembly depending on the dispersion concentration, which may affect cavitation behavior. Hemolytic activity and cytotoxicity experiments

revealed that the inclusion complex is biocompatible at the concentration as high as 1 mg/mL. Finally, the ability to lower cavitation threshold for histotripsy was tested, and it showed that it acts as desired nuclei sites for cavitation at low pressures than histotripsy, indicating that this new agent can be effectively used as a histotripsy agent.

ÖZET

EV SAHİBİ-MİSAFİR ETKİLEŞİMİ KULLANILARAK HİSTOTİRİPSİ AJANI GELİŞTİRİLMESİ

Tanzeel Ur Rehman

Biyomedikal Mühendisliği ve Biyoinformatik, Yüksek Lisans

Tez Danışmanı: Doç. Dr. Yasemin Yüksel Durmaz

Aralık, 2017

Histotripsi, mikrosaniye boyunda, yüksek frekanslı ultrason (US) sinyallerini kullanarak, akustik kavitasyon mekanizmasını ile mekanik olarak hücre parçalama tekniğidir. Bu US sinyalleri vucutta hâlihazırda çözünmüş olarak bulunan gaz baloncuklarından bir baloncuk bulutu oluştururlar. Bu bulutun yeteri kadar enerji kazanarak parçalanması sonucu içerisinde bulundukları dokuda da mekanik bir parçalanma/hasar oluşur ve bu prosesin gerçekleşmesi için yüksek basınç gerekmektedir. Yakın zamanlarda, içerisine perflorokarbon doldurulmuş nanodamlacıkların histotoripsi ajanı olarak kullanıldığı nanodamlacık ortamlı histotoripsi (NMH) bu yüksek basınç sınırlamasına çözüm olmuştur. Nanodamlacıklar histotripsi için mükemmel ajanlar olmalarına rağmen, sentezleri karmaşıktır ve polimer kimyası alanında tecrübe gerektirmektedir. Bu çalışmanın amacı, histotripsi için nanodamlacıklar kadar etkin çalışacak, ama üretimi çok daha kolay, büyük miktarlarda üretime uygun ve daha kolay ticarileşebilme potansiyeli olan yeni bir histortripsi ajanı geliştirmektir. Amerikan Gıda ve İlaç Kurumu (FDA) tarafından onaylamış ve ticari olarak temin edilebilen β-siklodekstrin (CD) ve perflorohekzan (PFH) bileşiklerinin ev sahibi-misafir etkileşimi ile inklüsyon kompleksin oluşturması ile, hidrofobik karakterdeki perflorokarbon siklodekstrinin hidrofobik kavitesine girerek, histotripsi sırasında kavitasyon oluşturacak çekirdek görevi üstelenebilir. Bu durum histotripsi uygulaması sırasında kavitasyon için gerekli eşik basıncının düşürülmesini sağlayacaktr.

PFH başarılı bir şekilde %98 etkinlikle siklodekstrinin hidrofobik kavitesine yerleştirilmiştir. Karakterizasyon çalışmalar inklüsyon kompleksinin oluşumunu desteklemiş ve PFH/CD oranına bağlı olarak bir CD kavitesine 2 tane PFH'nin girme olasılığını desteklemiştir. Bu inklusyon kompleksinin boyutu nanodamlacıklardan daha küçük bir değer olan 48 nm olarak ölçülmüştür, fakat

elde edilen komleksin suda dağıtılma konsantrasyonuna bağlı olarak kendi kendini daha büyük boyutlu parçacıklar halinde düzenlediği gözlenmiştir, bu durum histotoripside kavitasyon davranışını etkileyen bir parametre olabilir. Ayrıca hemolitik aktivitelerinin ve hücre içi sitotoksisitelerinin incelenmesi sonucu bu komplekslerin 1mg/mL gibi yüksek konsantrasyonlarda bile toksik etki göstermediği gözlenmiştir. Son olarak, histotripsi ajanı olarak kavitasyon eşik basıncını düşürebilme kapasitesi test edildiğinde, beklenen etkiyi gerçekleştirdiği, nanodamlacıklarda olduğu gibi kavitasyon eşik basıncını düşürdüğü gözlenmiştir.

Anahtar sözcükler: Histotripsi, ev sahibi-misafir etkileşimi, β-siklodekstrin, perflorohekzan.

Acknowledgement

First and foremost, I would like to express my sincere gratitude to my advisor Assoc. Prof. Dr. Yasemin Yuksel Durmaz for the continuous support of my M. Sc. study and research, for her patience, motivation, enthusiasm, and immense knowledge. I could not have asked for better guidance in this educational journey.

I would also like to thank the rest of my committee: Asst. Prof. Dr. Mehmet Ucisik and Assoc. Prof. Dr. Bunyamin Karagoz for their encouragement, insightful comments, and inspiring questions.

In addition, I thank my fellow labmate and friend Erhan Demirel for the stimulating discussions, hard work, and selfless knowledge shared during our research work.

Last but not the least, I would like to thank my family for always supporting my dreams and aspirations. They are the pillar of my life, and I am forever grateful to them for guiding me to a bright future.

Contents

List of Figures

List of Tables

Chapter 1

Introduction

Cancer is a set of diseases caused by the abnormal and uncontrolled division of cells [1]. The cells divide without stopping, and continue spreading and surrounding the area around the tissue. The whole body is made up of trillions of cells, and cancer can start in any of them because it is not specific to a particular body part. Normally, a cell grows, divides, and when its purpose is served, it ages and dies. When it comes to cancer cells, this process is altered. When a cell becomes abnormal, it gets old, but it does not die as it is expected. Additional cells are created as well, even though they are not needed as the existing ones did not die. These extra cells, once they start proliferating, do not stop, and cause excessive growths known as tumors. In 2017 only, more than 1.5 Million new cancer cases are expected with more than 0.6 Million deaths [2]. In 2016, approximately 23% of the total deaths in USA were caused by cancer [3].

Cancer staging, a process which provides information about the location and the size of the tumor, is one of the initial steps in the therapy. It also gives information about whether the tumor has spread to other organs or not [4] .Treatment decisions are made based on the information provided by staging. Although, removal of cancer by surgery, also known as oncological surgery, is known to be the oldest treatment for cancer, but it involves complex surgical procedures.

Most of these surgeries are followed either by chemotherapy or by radiation therapy, in which exhausts the patients too much, and includes affects like hair loss and intense weakness. Depending upon the cancer type and size, chemotherapy and radiation therapy are sometime used on their own without the surgery. Chemotherapy, basically, is just the use of any drug to treat any disease. It uses a drug to be injected in the body, and kills the cells. The biggest disadvantage of chemotherapy is that it cannot differentiate between healthy and cancerous cells [5]. Thus, it ends up killing both healthy and cancerous cells, causing sizeable weakness for the patient, and often causing death. Radiation therapy, on the other hand, uses high energy X-rays to kill the tumor. Again, the disadvantage is that it damaged the healthy cells around the tumor and it might end up damaging organs [6].

As science is advancing, new and advanced methods for the treatment of cancer are emerging. Immunotherapy, hormone therapy, and targeted therapy are some of these methods. In immunotherapy, the immune system of the body is strengthened so that it can fight cancer more efficiently [7]. The immune system can be boosted using different substances from the body, or compounds developed in the laboratory. The hormone therapy is currently in use for breast cancer. It works in an indirect way by making a hindrance for estrogen, and also, by limiting its occurrence in the body. Targeted therapy uses micro- or nano-sized particles to treat the tumor. These particles can carry drugs, DNA, and RNA etc. They can also be used with different image modalities for advanced results [8]. There are various types of micro and nanoparticles available, such as drug conjugates, dendrimers, vesicles, micelles, microbubbles etc. Imaging modalities which can be used with these are optical imaging, Magnetic Resonance Imaging (MRI), Radionuclide-based imaging, Computer tomography (CT), and Ultrasound (US) [8]. US was first used for medical purpose by psychiatrist and neurologist Karl Dussik in 1942, and it has been helping the medical field ever since [9, 10]. Although, initially, US became popular for its imaging capability in diagnostic medicine, recent advancements have allowed US to be used as a therapeutic device as well [9]. For therapeutic purposes, US was used to enhance the delivery of chemotherapeutic-, thrombolytic-, and gene-based drugs [11, 12, 13].

Along with aiding the drug delivery process, US contrast agents are now being developing to enhance its image contrast. Research has proven that US contrast agents can also be used as drug and gene delivery carriers [14, 15, 16]. They can be loaded with drugs or genes with targeting ligands on the surface, and imaged using US. Once the imaging is complete, the US frequencies can be altered to rupture the contrast agents, so that the drug can be released locally onto the tumor [17, 18].

Other than drug delivery enhancement, and use of US sensitive contrast agents, US has also been distinguished in treating cancer tumors through mechanical cell ablation techniques. The basic principle involves using US frequencies to increase the temperature of the tumor to cause either coagulative necrosis or cavitation. Radiofrequency ablation (RA), laser ablation (LA), high-intensity focused ultrasound (HIFU), and histotripsy are some of the mechanical cell ablation techniques. Histotripsy, the newest technique, was developed about 10 years ago, and it uses acoustic cavitation as the primary mechanism. A histotripsy transducer releases very high frequency US pulses focused on a region of a tissue. The gas pockets in the tissue acts as the nuclei for cavitation and forms a highly dynamic cluster of microbubbles. When these microbubbles ruptures, it releases energies high enough to fractionate the cell. Usually, histotripsy required high pressures to turn these gas pockets into a microbubble cloud, usually ranging from 28 MPa to 30 MPa. With this much pressure, there is a risk of rupturing the normal tissue without the tumor.

After recent advancements, a new type of histotripsy emerged known as Nanodroplet Mediated Histotripsy (NMH). This NMH uses small polymer nanodroplets which encapsulate perfluoropentane (PFP) [19]. Once in the tumor, instead of regular gas pockets, these nanodroplets act as the nuclei for bubble cloud formation, which then leads to cavitation [20]. These nanodroplets were reported to bring down the high cavitation pressure from 28MPa to 7 MPa, thus, solving the risk of damaging normal tumor free tissues [19]. Despite the fact that these nanodroplets work perfectly for NMH, the synthesis of these nanodroplets contains multiple steps. Advanced skills and expertise in polymer chemistry are needed for the synthesis of a tri-block polymer which is the main component of

the nanodroplets. Additionally, these nanodroplets are currently the only agents available and produced for NMH. Thus, there is a need for a new, easy to synthesize, and user-friendly histotripsy agent.

In this study, the limitations of the nanodroplets are addressed, and a new histotripsy agent is manufactured. It includes a simple host-guest chemistry using β-cyclodextrin (BCD) and perfluorohexane (PFH). Both the agents are commercially available and approved by the Food and Drug Administration (FDA). The method used for the synthesis is relatively easier, economical, efficient, and more suitable for commercialization. The goal of this study is to present a new histotripsy agent which is as efficient as the nanodroplets, but has the upper hand when it comes to ease of generation.

Chapter 2

Imaging and therapy agents for ultrasound applications

2.1 Imaging agents for ultrasound applications

US is basically a sound wave at frequencies exceeding the audible band [5]. In the field of diagnostic medicine, these waves are transmitted to a part of the body. According to difference in the densities and absorption of components in the body, these waves are reflected back and an image is generated [21]. It has been decades since US has been used as an imaging device and helping the medical field [10]. Not only it provides a real time image, also it is completely harmless and painless. The patients are not exposed to any type of radiations. US scans does to include any needles or injections. US has been used for pregnancy tests for more than 40 years now, and there has not been any report to suggest that it causes any harm to the patient, embryo, or fetus since.

Compared to other imaging modalities, US is less expensive than other devices. Also, it is easier to identify soft tissues in an US image, which are not visible in X-ray images. To make the US image quality better, different polymeric microbubbles are used as contrast agents. These are injected into the body
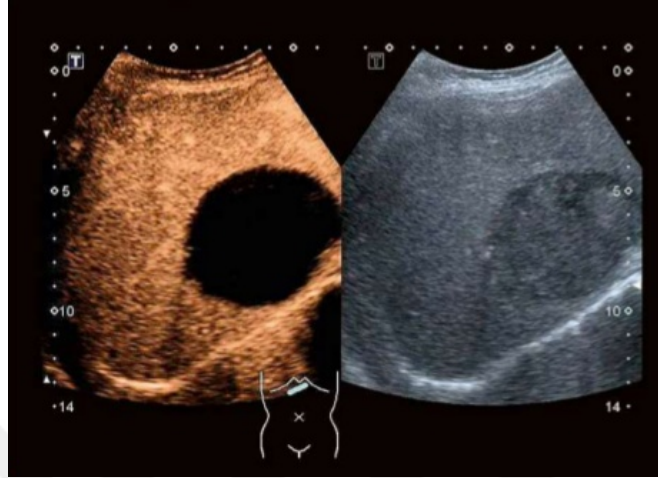
Figure 2.1: A comparison of an US image before and after the addition of the contrast agents.

before the US scans, and they provide considerable contrast in the images after the injection. Figure 2.1 shows two US images, the left image is taken before the addition of the contrast agents. Compared to that, a clear enhancement in the contrast can be seen in the picture on the right which was taken after the injection of the contrast agents.

Initially, the microbubbles produced encapsulated air inside them. Later microbubbles were developed containing fluorinated gas, such as perfluoropentane (PFP), perfluoropropane (PFR), and perfluorohexane (PFH) etc. These are surrounded by either a polymer, lipid or a protein [22]. The microbubbles have a high compressibility compared to the tissue surrounding the bubbles. This gives a rise to the acoustic impedance and the microbubbles oscillates, which in turn produces nonlinear acoustic radiations ad a medium range of US frequencies [23]. It is this phenomenon that provides a higher contrast in the region which has these microbubbles [24, 25].

Currently, many of these microbubbles are commercialized and being used all over the world. Albunex was one of the first commercialized microbubbles which contained an air core surrounded by albumin. Fluorinated gas encapsulated microbubbles were developed and commercialized later. Optison and Definity were developed which encapsulated PFR and had a shell of protein and phospholipid,

respectively [26].

More work had been done on these contrast agents to lower the size of these microbubbles to nano width. It was observed that lowering the size of these microbubbles lowers the contrast enhancing capabilities of the microbubbles. On the contrary, a new gateway was open where these could be used as therapy agents. Since then, US has been used as a diagnostic device as well as a therapeutic device. Present day, therapy using ultrasound can be classified in to three categories. Ultrasound for drug delivery using ultrasound, ultrasound based thernostics, and therapy using mechanical ablation techniques [27].

2.2   Drug delivery using ultrasound

US has shown evidence to raise the thrombolytic efficacy of urokinase [28]. This phenomenon can occur due to localized cavitation or the weakening of the clot by the use of US. Also, this will increase the penetration of the drugs into the cells or the tumor [29, 30]. Furthermore, it has been shown that the presence of microbubbles enhances this phenomenon. When the US is exposed to the body in the presence of the microbubbles, they produces pores on the surface of the cells through which the drugs can penetrate easily [31, 32].

If the tumor is small, ultrasound is used to cause hyperthermia to the tumor specific region. With the use of high intensities ultrasound, the temperature of the tumor is elevated high enough to go through coagulation [33, 34]. By this, the tumor is damaged and can also be killed by minimal damage to the normal tissues surrounding the tumor [35, 36].

Another way to enhance the delivery of chemotherapeutic drugs is by using lower intensities of the ultrasound. This increases the temperature moderately and amplifies the cytotoxity of the chemotherapeutic drugs [12, 11]. US has been tested to enhance the drug delivery in a number of biological and clinical trials. Unger et al. performed experiments using microbubbles which encapsulated a

drug filled layer of soy bean oil and the drug paclitaxel [37]. He concluded that the microbubbles enhances the drug delivery and helps to produce pores on the cell surfaces for easier penetration of the drug. Guzmen et al. also conducted experiments to quantify the molecular uptake of celcein in prostate cancer, and also tested aortic in smooth muscle cells. He investigated the heterogeneity of the cavitation and factors of that enhances the cell uptake [38, 38]. Literature also shows that microbubbles have been used with Doxorubicin and colloidal particles for enhanced cell uptake [39, 40].

2.3   Ultrasound based theranostics

The term theranostics was recently formulated to specify the ongoing research and efforts going on which were focused on to bringing together the advantages of diagnostics and therapy to form a single agent [41]. Once the size of the microbubbles was lowered, they were known as nanoparticles. Development of these nanoparticles opened a new portal for the therapeutic paradigm. It joins together the imaging as well was therapeutic functions giving rise to a theranostic agent capable of diagnosis, drug delivery and monitoring of therapeutic response [41].

To date, many different types of theranostic agents have been produced with different surface chemistries. It is because of their surface chemistry that pharmaceutical and chemotherapeutic drugs can be loaded inside the core. Nanoparticles with different surface chemistries are available ranging from iron oxide, gold, quantum dots, silica and carbon nano tubes.

Zhang et al. developed pH sensitive iron oxide particles which contained methotrexate, a chemotherapeutic drug, onto the surface [42]. These particles were tested in vivo which revealed these particles enters the cells and upon reaching in the lysosomes, the drug is released due to the pH difference and because of the presence of proteases. Similarly, Hwu et al. demonstrated the use of paclitaxel drug onto the surface of these iron oxide nanoparticles [43] Other than

these, there are many other examples present which shows the use of doxorubicin as well [44].

Apart from drug delivery, RNA and DNA can also be delivered to the cells. This technique is knows as gene delivery or gene therapy. It was in 1996, that Kim et al. used the US to transfer the plasmid DNA to a variety of cells [45]. Also, they performed an in vivo experiment where they used albumin based theranostic agents to load plasmid DNA and transferred them to rat knees [30]. There are more examples in the literature with more work on delivering plasmid DNA, and also delivering DNA to heart and lungs of mice and rats [46, 47, 48, 49, 50, 51, 52, 53, 14].

2.4   Therapy using mechanical ablation techniques

Ablation literally means chipping off, or vaporizing a material. In biological terms, mechanical cell ablation is referred to a technique in which a tumor is ablated locally, using different instruments, with minimal damage to the surroundings [54]. With the advancements, the combination of ablation with imaging techniques like ultrasound makes it more focused and efficient. Image guided ablation has a huge potential, and is an adroit alternative for the treatment, especially when the patient cannot undergo a surgical treatment [55, 56, 57].

Another advantage of using the ablation technique is that after the ablation, the remaining debris in situ may work as tumor antigens to the immune system. This might turn into a process known as the Abscopal effect [58]. This mean that the ablated tumor debris will work as an in situ cancer vaccine which would stimulate systemic immune responses towards metastases present everywhere in the body [59]. There are different types of cell ablation techniques available like radiofrequency ablation (RFA), laser ablation (LA), high-intensity focused ultrasound (HIFU), and histotripsy. Each of these techniques will be discussed

one by one below.

2.4.1 Radiofrequency ablation

Radiofrequency ablation (RFA) is an image guided, minimally invasive treatment for cancer. A thin needle electrode is inserted in the body near the tumor and alternating current at about 400 MHz frequency is passed through it. This results in frictional agitation of the molecules and generates heat, knows as the joule effect [60, 61]. This process creates a focal heat on the tumor and kills the cells surrounding the electrode, with little heat transferred to tumor free areas [62, 63]. Figure 2.2 displays how the RFA works using a US on the left and, on the right, it shows an RFA needle electrode is shown. This technique has advantages like option for local treatment. Also, it can be used in supplement with chemotherapy to provide a better result. When used with chemotherapy, it also prolongs the time without toxicity in the body [64]. Image modalities such as US, MRI or CT can be used as a guide for RFA .However, RFA needs to be operated by a well-trained personnel preferably with a high quality device as well. Additionally, if the tumor size is larger, the efficiency of RFA decreases [65].
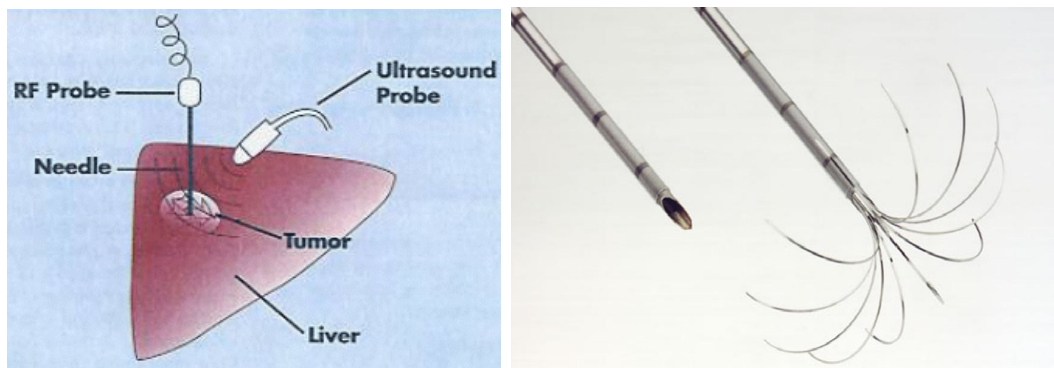
Figure 2.2: The working of the RFA (left). The needle electrode used in RFA (right).

2.4.2 Laser thermal ablation

Laser Thermal Ablation (LTA) has not been used as much as RFA but its results as good enough to be compared with RFA. Research has proven that LTA can be used to fully ablate a tumor which is eligible for thermal ablation [66]. In LTA, a high energy laser radiation is delivered through laser optic fibers to the tissue. Due to the absorption of laser, temperatures as high as 150°C can be reached. This much high temperature can cause coagulative necrosis [67, 68]. Due to a higher penetration of light in the near infrared spectrum, Neodymium:Yttrium Aluminum Garnet (Nd:YAG) and diode lasers of wavelengths 1064 nm and 800-980 nm, respectively, are most commonly used.

Usually, a single optical fiber is used for ablation, which creates a thermal lesion of about 15 mm [66]. A beam splitting device can be used as well, creating two beams with a single source. Also, a multi-source device can be used, which allows four fiber optics to be used at the same time, this results in a higher ablation area [69, 70]. Although LTA produces good results, there is still a risk of damage to the surrounding area due to extensive working temperature of the laser [71, 72].

2.4.3 High intensity focused ultrasound ablation

As everyone knows, today the application of US is not limited to diagnostics purposes only. They are also used to treat the diseases in multiple ways. High intensity focused ultrasound (HIFU) was developed in the 1940s but it didnt reach its pinnacle until recent developments. Now HIFU is one of the best noninvasive and extracorporeal technique. The best feature among many others is that there is no need for a lesion, or any penetration through the skin. HIFU operates from above the skin [73]. Figure 2.3 shows how the HIFU bean passes through the skin and focuses onto the tumor and induces tumor necrosis.
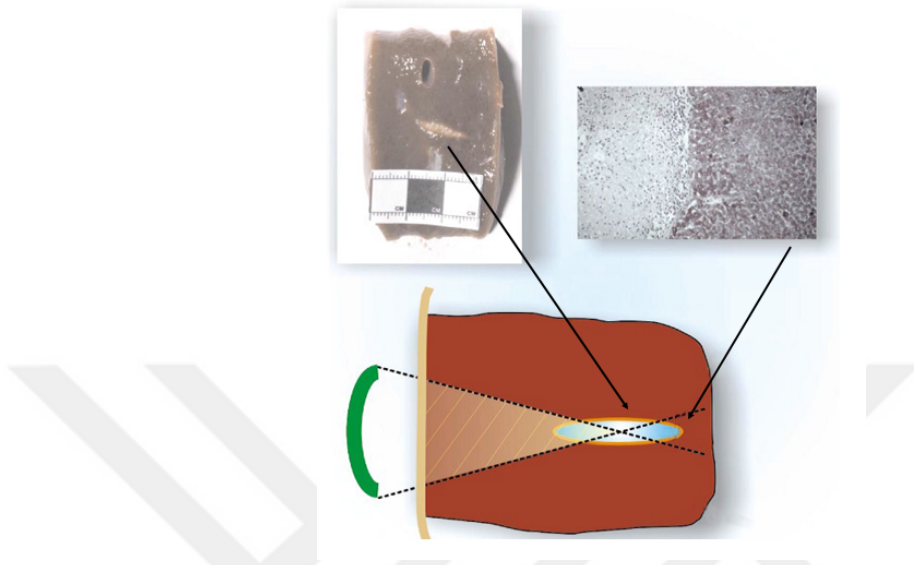
Figure 2.3: HIFU delivering a focused US beam to the tumor from outside the skin and a thin layer between dead and alive cells can be seen.

HIFU works on the same principle of a typical US. HIFU uses ultrasounds of higher intensities, 100-10,000 W/cm^2, focused at a specific region using the special probe. Figure 2.4 shows the transducer and the imaging probe used in a HIFU. These focused US increases the temperature of the tumor within 1 second. When the temperature of the tissue is rapidly increased above 60°C for one second, it ruptures instantly via coagulation necrosis [73]. This cell death via thermal effect is the primary mechanism of HIFU.

Mechanical effect is the secondary mechanism of HIFU. It works by inducing cavitation, radiation force, and micro-streaming using acoustic pulses of very high intensities. When an ultrasound wave of high intensity propagates though the tissue, due to the compression and expansion of the tissue, a gas cavity is formed in the acoustic field, this is known as cavitation.

A cavitation can be classified in two types, stable and inertial cavitation [74]. A stable cavitation occurs when a low pressure acoustic wave passes through the tissue. Whereas, an inertial cavitation is induced using high pressure acoustic waves which causes the bubble to oscillate aggressively and it increases in size. After reaching the resonance size, the bubble collapses resulting in very high

pressure and temperature, 20,000 to 30,000 bars and 5000 K, respectively, in the microenvironment [74].

Although, HIFU is advancing in the field of treating cancer, and the results are very impressive, but it has a few limitations which needs to be addressed. Firstly, HIFU is incapable of predicting and controlling the formation of the lesion. Secondly, the cavitation might occur in the normal tissue as well. Finally, it has a poor tissue contrast with a limited field of view which makes it difficult to use [75].
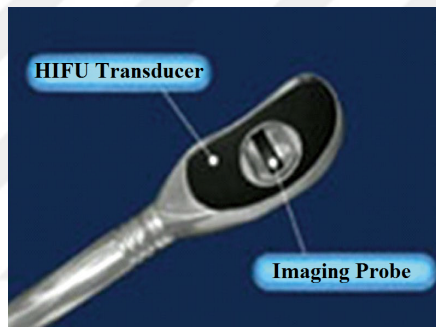
Figure 2.4: An imaging probe and a transducer used for HIFU.

2.4.4   Histotripsy

Histotripsy is a recently developed technique which is completely non-invasive and extracorporeal [76]. It uses very short (15 —20 s), high intensity (500 MHz —1000 MHz) US pulses focused on the tissue. This produces a cloud of cavitation bubble in the tissue which oscillates and builds up the pressure. Once the negative pressure is raised above the critical threshold pressure of around 28 MPa, this bubble cloud bursts and ablates the tissue surrounding the cloud [76, 77].

The histotripsy works on the mechanism of acoustic cavitation. The alteration in the US pressure form microbubbles in the human tissue. Once the energy level is high enough, the microbubble activities fragment and subdivide tissue, which results in cellular destruction. Histotripsy has some important advantageous
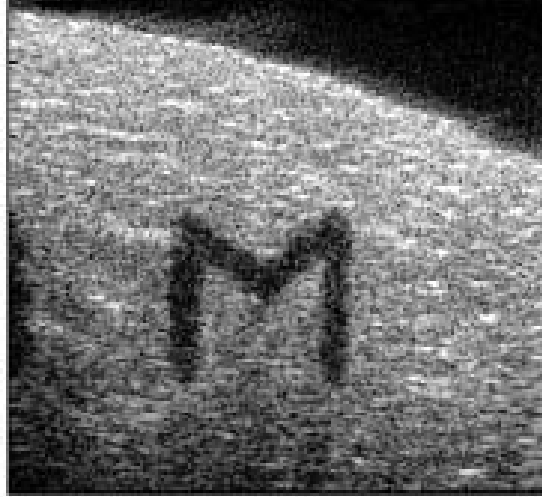
Figure 2.5: The letter 'M' drawn on a tissue phantom using histotripsy.

points when compared to non-invasive thermal therapy. First of all, microbubbles are clearly visible through US imaging, so the operator can see the targeted volume. Additionally, the US imaging provides real-time feedback of the energetic microbubble activities and the cellular destruction, which allows for a more transparent treatment. Finally, this technique is very precise, and allows for the treatment to be performed in a controlled environment. Figure 2.5 shows an example of the precision of histotirpsy, as it shows a letter 'M' made on the tissue phantom using the histotripsy. A clear depth can be seen where the phantom is ablated.

2.4.5 Nanodroplet mediated histotripsy

NMH is mediated by polymer nanodroplets which contains PFP inside them. It has been proven that using these PFP filled nanodroplets under high frequency ultrasounds vaporizes and form gas bubbles. Once these gas bubbles are formed, histotripsy uses these gas bubbles for cavitation which can be achieved at a significantly lower threshold pressure or 7 MPa [20]. This NMH approach takes advantage of the significantly reduced cavitation threshold of the nanodroplets localize allowing cavitation to be selectively generated only in regions where nanodroplets [65]. NMH has the potential for selective ablation of tumors given the

small size (100 —400 nm) of the synthesized nanodroplets, which enables their diffusion across the leaky tumor vasculature and preferential accumulation in the tumor tissue [78]. Evidence was provided that this NMH can be used to create well-defined ablation similar to that obtained with histotripsy, but at significantly lower pressure, and has also indicated the potential to use NMH for simultaneous multifocal ablation [20].

Durmaz et al. showed that because of the small size of the nanodroplets, the histotripsy threshold pressure, needed for cavitation, dropped significantly [76]. They claimed that encapsulating the nanodroplets with PFP will further decrease the cavitation threshold pressure making NMH totally non-invasive and safe for the normal tissues. The effect of adding PFP can be seen in Figure 2.6. It shows how a 2-cycle histotripsy pulse (20.7 MPa), with a pulse repetition of 10 MHz, generates a bubble cloud which leads to ablation. This ablation area increases with the increase in the percentage of PFP. In another experiment, they showed that same results can be achieved by the using the PFP encapsulated nanodroplets at 11.0 MPa. This result is shows in figure 2.7.
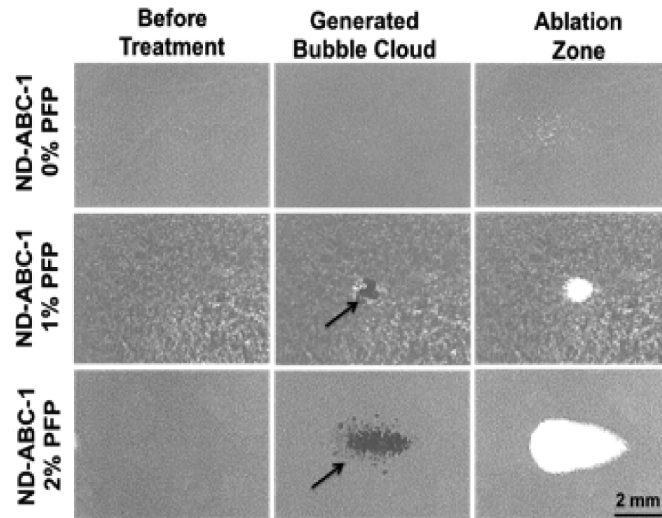
Figure 2.6: The effect of 2-cycle histotripsy pulse (20.7 MPa) with a pulse repetition frequency of 10 MHz on the nanodroplets with different PFP loading and embedded with RBCs in agarose gels.

Furthermore, it was also hypothesized that the small size of the nanodroplets would help them to accumulate inside the tumor through the EPR effect. Additionally, targeting ligands can be attached on the surface of the nanodroplets and they can be directed towards a specific organ in the body. Moreover, these nanodroplets also function as an US contrast agents. The encapsulated PFP inside them is, which is approved by the FDA. This allows the tumor to be easily seen through the US in real-time and also guides the histotripsy throughout treatment.
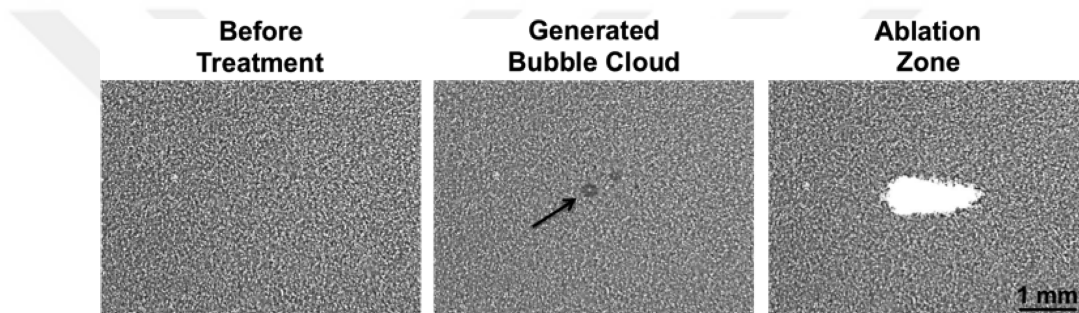
Figure 2.7: The effect of 2-cycle histotripsy pulse (11.0 MPa) with a pulse repetition frequency of 10 MHz on nanodroplets containing 1 —2 % PFP.

Although, the NMH is works in an excelling way, the synthesis of the polymer and fabrication of the nanodroplets is a complex part. The nanodroplets are composed of a tri—block copolymer which has to be synthesized in the lab and requires advanced skills and expertise in polymer chemistry [19]. Figure 2.8 shows a nanodroplet after complete synthesis of tri—block copolymer, PFP encapsulation and crosslinking. Once the tri-block copolymer is produced, it is then used to fabricate the nanodroplets encapsulating the PFP. Other than this, currently only this nanodroplets is available for NMH. There is no other type of droplets, or any other agent that can be used to provide the same results of lowering the threshold cavitation pressure of NMH.

Thus, there is an immediate need of new, innovative agents that can be used as histotripsy agents. We hypothesize that there is a simple and fast way to achieve new kind of histotripsy agents which are easy to produce and are cost effective. It uses BCD, a 7 sugar unit molecule, which has a cone like structure can be filled up with PFH to produce the same effect as the nanodroplets using a rather simple method. Both of these materials are approved by the FDA and

16
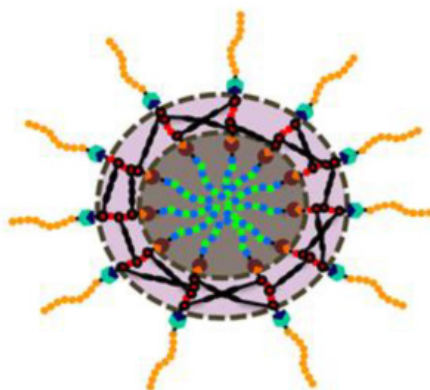
Figure 2.8: A PFP encapsulated nanodroplet with a cross-linked tri-block copolymer.

commercially available. The method used for the synthesis is relatively easier, economical, efficient, and more suitable for commercialization.

2.5   Host—guest inclusion complex

The origin of host-guest chemistry dates back in to 1987 when three scientists named Lehn, Cram, and Pedersen won the Nobel Prize on the discovery of the host-guest systems [79]. It gained much attention because this host-guest interaction utilized noncovalent interactions, such as, hydrogen-bonding, van der Waals forces, $\pi - \pi$ stacking interactions, and electrostatic interactions. During the past decade, numerous applications have been discovered in which host-guest interactions plays a vital role. Host-guest interactions contribute to the field of functional materials, electronic devices, catalysis, nanomedicine, and so on [80, 81, 82, 83].

The host-guest chemistry involves, the 'host' molecule encapsulates the 'guest' molecule through noncovalent interactions. Usually, the host has a macrocyclic structure, and thus has special physical, chemical, and biological properties. In

the field of biomedicine, cyclodextrins (CD), cucurbituril (CB), and calixarene (CA) are the most common host molecules used.

The 'guest' molecule can be chosen from a lot of different options. Mostly, chemotherapeutic drugs are hydrophobic and encapsulated in the host molecules for better solubility. Gene delivery also benefits from host-guest interaction and DNA and RNA can also be delivered using the hosts. There are studies that showed promising results from these interactions. Jing et al. worked on the encapsulation of paclitaxel, a chemoterapeutic drug, in CD as a host[84]. Wheate et al. showed how CB can be used to lower the toxicity of anticancer drugs and the interaction with DNA [85]. It was also reported to have increased the solubility of albendazole by 2000-folds [86]. For CA, it has been reported to use the poorly soluble drug, mycophenolate mofetil, with CA and was made soluble [87]. Also, reports of using CA to increase the solubility of carvedilol and lamotrigine have been seen [88, 89].

Although work is being done for all the host molecules, but CD are one of the most famous host molecules. CDs are explained in detail below.

2.5.1 Cyclodextrin

CDs, which are also known as cycloamyloses, belong to the family of cyclic oligosaccharides (sugar units) and they are bound together in a circular ring. They have unique physical properties, and their outer surface is hydrophilic but the internal cavity is hydrophobic [90]. CDs are mainly characterized in three forms based on the number of glucose monomer which ranges from six to eight. α-cyclodextrin (ACD, alpha cyclodextrin) contains six sugar units, β-cyclodextrin (BCD, beta cyclodextrin) consists seven sugar units whereas γ-cyclodextrin (GCD, gamma cyclodextrin) accommodates eight sugar units in a circular shape. Each of these CD differ from each other in physical dimensions. Figure 2.9 gives a pictorial representation of the difference in the cavity dimensions of each of these CDs, also structural shape of the three CDs.
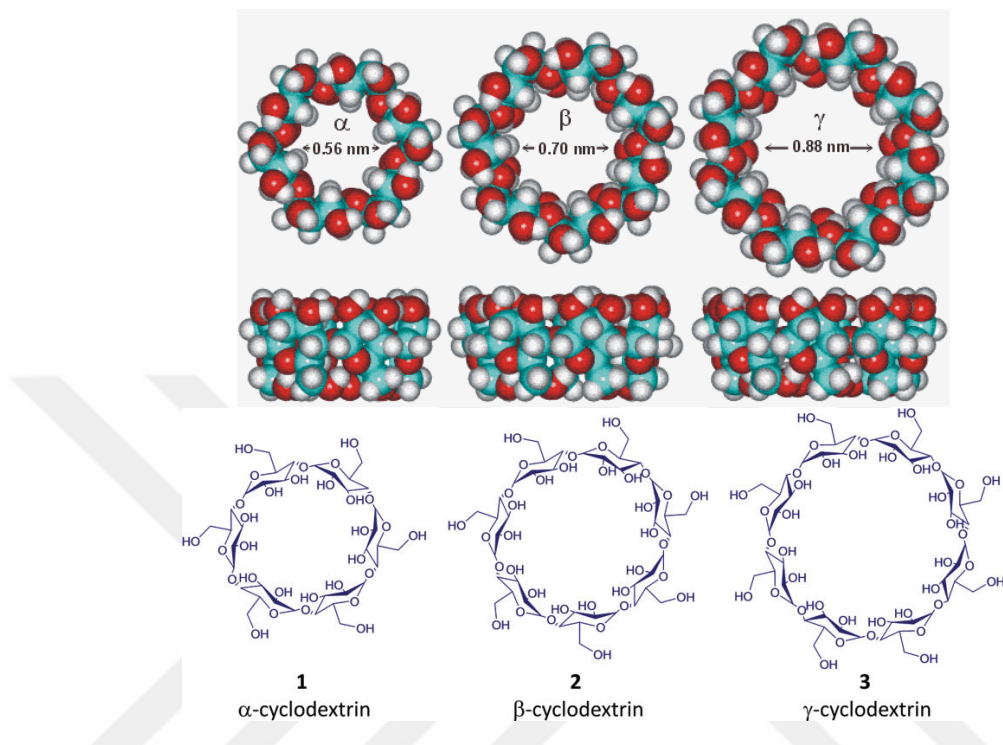
Figure 2.9: Comparison of the inner diameter of alpha, beta and gamma cyclodextrins, also showing the structural shape of the cyclodextrins.

Even with the lowest solubility, BCD is the most famous of the three CDs and are the most thoroughly investigated of the CDs. Studies have shown that BCD has better dissociation characteristics than other CDs, when complexed with many drugs, including nonsteroidal anti-inflammatory drugs (NSAIDs) [91]. By complexing an NSAID with a BCD, a number of NSAIDs can be made soluble and their dissolution rates can be increased.

BCD is known for its use in the food industry, chemical industry and in pharmaceutical industry for drug delivery [92, 91]. In the food industry, BCD is used for the preparation of cholesterol free products. Oil, being hydrophobic, easily slides into the hydrophobic cavity of the BCD and these are later removed to produce and oil free product. For chemical industries, BCD is used to make aerosols. The Table 2.1 lists different physical dimensions of each of the CDs.

The pharmaceutical industries takes the most advantage of the CDs because it is recognized as safe and is approved by the Food and Drug Administration

Table 2.1: A comparison of the physical properties of the CDs.

CDs	Molecular weight (g/mol)	Outer dia (nm)	Inner dia (nm)	Solubility in water (g/kg)
ACD	972	1.52	0.45	129.5
BCD	1134	1.66	0.60	18.4
GCD	1296	1.77	0.75	249.2

(FDA) [93]. Because of the hydrophobic cavity of the BCD, hydrophobic drugs can be inserted in the cavity and thus are soluble in water. BCD has the ability to undergo host-guest interactions resulting in the formation of inclusion complexes. In these inclusion complex, the hydrophobic guest particle goes inside the hydrophobic cavity of BCD. By this, the hydrophobic particle can be made soluble, and can be delivered to any part of the body.

Figure 2.10 shows the 3-D structure of BCD, also showing the hydrophobic cavity. Since, the hydrophobic cavity can interact with any hydrophobic material, we intent to react it with PFH to form an inclusion complex (IC). PFH, a type of perfluorocarbon, and forms an IS which is stable at room temperature and can be used as a histotripsy agent.
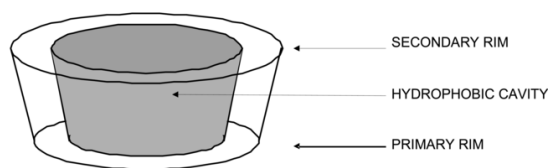
Figure 2.10: A 3D structure of BCD showing its hydrophobic cavity.

2.5.2 Perfluorocarbons

Perfluorocarbons (PFC) belongs to the family of organofluorine and has the formula CxFy. PFCs are made up of stabe C-F bonds and are chemically inert, therefore, they do not metabolize in the body. They can be removed from body by simple inhalation [94, 95]. There can be many types of PFC, such as perfluoroalkanes, perfluoroalkenes, and perfluoroalkynes etc. They are used in many different

industries. PFCs are used as refrigerants, solvents, fluoropolymers, gas/oxygen carriers, and also in the field of medicine as anesthetics and liquid ventilation [96, 97]. Recently, PFCs have gained much popularity due to its potential as the use of contrast agents in medical devices like MRI, CT, and US [98].

PFH being liquid at room temperature, with a boiling pint of 56 °C, has advantage to be used at room temperature. Moreover, having a small linear chain is suitable for reactions like host-guest interactions forming inclusion complex. Figure 2.11 shows the linear structure of PFH and also the molecular formula of PFH.

Currently, because of its ability to dissolve oxygen in high amounts, it is used in the liquid ventilation systems in case of lung diseases or lung failure [99, 100]. In the late 80s and early 90s, PFH began to gain popularity as a contrast agent for US and other medical devices [101, 102]. Since then there has been immense research on PFH being used as contrast agents for US and it has been very successful.

As histotripsy uses high frequency US waves, the use of PFH as inclusion complex is very effective. Due to its lower boiling point, PFH vaporizes at lower pressures and forms a bubble cloud which leads to cavitation. This was also confirmed by Vlaisavljevich et al. that PFH works better in histotripsy rather than PFP [76]. Furthermore, it also acts as a contrast agent for the US. This helps in the real-time imaging and also to locate the tumor more easily. Once in the US, it is seen that all the inclusion complexes containing PFH are attached or accumulate into the tumor, and cavitation can be achieved leading to tumor ablation without any damage to the normal cells.
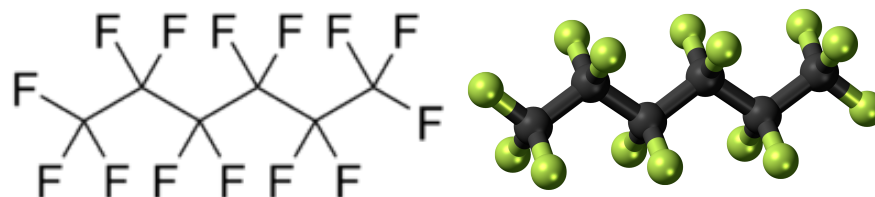
Figure 2.11: A 2D and 3D structure of PFH.

2.6 Hypothesis

We hypothesize that we can obtain an inclusion complex as histotripsy agent using host-guest interaction between BCD and PFH. We expect it to lower cavitation threshold of the histotripsy, by acting as a histotripsy agent, and by working as effective as nanodroplets, whereas its production will be more user friendly, economical, practical and faster than nanodroplets. BCD, being an FDA approved product, with its hydrophilic outer surface and hydrophobic inner cavity can accommodate at least one hydrophobic PFH molecule forming inclusion complex. We expect them to have smaller size than nanodroplets that can penetrate deeper into tumor tissue. Since primary face of BCD still will be available for desired modification, this agent might have potential to be easily targeted towards specific cell line. This inclusion complex will also have an ability to form a self-assembly depending of the concentration in the dispersion that could be effect on the cavitation threshold.

Chapter 3

Experimental section

3.1   Materials

β-Cyclodextrin (BCD, Sigma-Aldrich,   97%), tetradecafluorohexane (PFH, Sigma-Aldrich, 99%), dimethyl carbonate anhydrous (DMC, Alfa Aesar, 99%), potassium carbonate anhydrous (K_2CO_3, Sigma-Aldrich, 99.99%), anisole anhydrous (Sigma-Aldrich, 99.7%), N,N-dimethylformamide anhydrous (DMF, Sigma-Aldrich, 99.8%), dimethyl sulfoxide (DMSO, Merck 99%), acetone (Sigma-Aldrich, 99.5%), diethyl ether anhydrous (DEE, Sigma-Aldrich, 99%), sodium chloride anhydrous (NaCl, Wisent Bioproducts, 99%), Phosphate Buffer Solution (PBS, Multicell, Wisent Inc.), ethanol (Sigma Aldrich, 99.8%), Dulbecco's Modified Eagle's Medium (DMEM, Multicell, Wisent Inc.), Fetal Bovine Serum Advanced, Heat Inactivated (FBS, Capricorn Scientific GmbH), L-Glutamine, 200 mM solution (29.23 mg/mL in 0.85% NaCl) (Multicell, Wisent Inc.), Penicillin streptomycin solution (Multicell, Wisent Inc.) Trypsin EDTA (0.25%trypsin) in HBSS, 1X (Multicell, Wisent Inc.) Trypan Blue solution, 0.4% (Sigma Aldrich).

3.2 Methods

3.2.1 Preparation of β—cyclodextrin and perfluorohexane inclusion complex

The first step in the preparation of BCD—PFH inclusion complex (IC) was to optimize the experimental conditions in order to obtain an IC with the highest efficiency. Therefore, 50 mg CD (4.4 X 10^{-2} mmol) was mixed with 1 mL double distilled water (Direct—Q 3 Ultrapure Water System, LabRepCo) in 4 different vials. The solutions were stirred at 80°C until complete dissolution of CD. Afterwards, the temperature was slowly cooled down to 45°C. Once 45°C was obtained, different molar ratios of PFH (1, 2, 20, and 50 folds) were added to different solutions. After stirring the solutions overnight at 45°C, they were kept in a fridge at 4°C for one hour followed by centrifuge (Thermo scientific, MicroCL 21R) at 5000 rpm, for 10 min. The supernatant was decanted, and the precipitated was dried under vacuum. The dried ICs were stored at 4°C for further use and for characterizations.

3.2.2 Methylation of β—cyclodextrin

BCD was randomly methylated using the procedure described in Gan et al.[103] Briefly, 3 g CD (2.64 mmol) was dissolved in 60.0 mL DMF in a two-necked round bottom flask connected to a condenser on the top. After complete dissolution of BCD, 8.6 g of K_2CO_3 was added to the solution. 8.0 mL of DMC was added, as well, drop-by-drop and stirred overnight at room temperature. Subsequently, the catalyst was removed by centrifuging the solution at 2000 rpm for 5 minutes. The solvent and surplus DMC were separated from the solution by vacuum distillation during which the residue turned into a syrup-like concentration. Methylated β—Cyclodextrin (MCD) was then precipitated from acetone, and rinsed three times using diethylether. MCD was then filtered, and dried under vacuum. The dried MCD was stored at 4°C for further use and for characterizations.

3.2.3 Preparation of methylated β—cyclodextrin and perfluorohexane inclusion complex

For the preparation of MCD-PFH IC (MIC), 50 mg MCD was dissolved in 1 mL double distilled water at room temperature in three separate vials. MCD was readily dissolved in water. Different molar ratios of PFH (5, 10, 50 folds) were added to each vial, and the solutions were stirred overnight. After 24 hours, the solutions were centrifuged at 5000 rpm, for 10 min. The supernatant was decanted, and the precipitate was dried under vacuum. The dried MIC was stored at 4°C for further use and characterizations.

3.2.4 Hemolysis

To study the hemolysis profile of the IC and MIC, 4 mL of a blood sample was collected from a volunteer. The blood was centrifuged (Thermo scientific, SL 16R) at 3500 rpm for 5 minutes. With a permanent marker, a line was marked at the point where red blood cells (RBCs) were separated from plasma, and also, at the maximum height of the plasma. The plasma was then removed, and 0.15M saline solution was added until the upper mark. The saline solution and RBCs were mixed gently followed by centrifuge again using the same protocol. This procedure was performed to rinse the RBCs. It was repeated three times. After the third rinsing of the RBCs, the saline solution was removed using centrifuge, and it was replaced with 100 mM phosphate buffer saline (PBS) until the same mark. This was the stock solution for the experiment. The working solution was prepared by 10% dilution of the stock solution. More specifically, 1 mL of the stock solution was taken in a 15 mL falcon tube, and 9 mL PBS was added and mixed gently. In a 2 mL Eppendorf tube, 200 L of the working solution was mixed with solutions of BCD, MCD, IC, and MIC, each with concentrations of 1.0 mg/mL, 0.5 mg/mL,and 0.1 mg/mL, all prepared in 1 X PBS. A volume of 1 mL was obtained in all the Eppendorf tubes. A positive control containing a solution of Triton X, and a negative control with only RBCs in PBS were also tested. The tubes were gently shaken so that the RBCs mix with the solutions

of the compounds. Afterwards, each solution was prepared as a triplicate. The solutions were placed in a water bath at 37°C for one hour. The solutions were then again centrifuged at 5000 rpm for 5 minutes. Both the intact and ruptured RBCs were accumulated at the bottom in the form of a pellet. The supernatant, on the other hand, contained the released hemoglobin from the ruptured RBCs. This supernatants absorbance was measured at 541 nm using a 96 well plate reader (SpectraMax® i3). The percentage hemolysis was calculated according to the following equation:

$$\% \, Hemolysis = \frac{Absorbance \, of \, sample \, - \, absorbance \, of \, negative \, control}{Absorbance \, of \, positive \, control} * 100\%$$

(3.1)

where negative control contains only the RBCs with PBS, while positive control contains RBS with PBS and triton X.

3.2.5 Cell toxicity studies

3.2.5.1 General cell culture procedure

Toxicity of BCD, MCD, IC, and MIC was investigated as a function of concentration using the MTS assay. The procedure was performed with full protocols of cell culture. 15 minutes prior to the start, all the liquids, including the medium and PBS, were placed in a water bath at 37°C. Meanwhile, the fume hood (Thermo Fisher, Maxisafe 2020) was cleaned using 70% ethanol. All the liquids from the water bath were sprayed with 70% ethanol and transferred to the fume hood.

Frozen human embryonic kidney cells (HEK-293T) were taken, and quickly melted by hands. In a 15 mL falcon tube, 10 mL Dulbeccos modified eagle medium (DMEM) was added, as well as the melted cells. It was then centrifuged at 1000 rpm for 5 min. After centrifuge, the cells were in form of a small pellet at the bottom of the tube. The medium was removed slowly without disturbing the

cells, and 5 mL of the growth medium (DMEM + 10% FBS+10% L-Glutamine + 5% penicillin streptomycin solution) was added to the cells. A T25 cell culture flask was prepared. The name, cell type, date, and passage number were written on both sides of the flask. 5 mL of the same growth medium was added to this cell culture. The 5 mL solution of cells from the falcon vial was transferred to this T25 flask so the total volume was 10 mL. This flask was sealed with a cap, and then viewed under a microscope (Zeiss Primo vert) to see if the cells are transferred successfully or not. After confirming successful transfer, the flask was placed in an incubator (Thermo Scientific, Forma Steri-Cycle CO^2 Incubator) at 37°C, and 5% carbon dioxide (CO^2).

After 48 hours, the medium of the cells was changed. PBS and growth medium were placed in a water bath at 37°C prior to the use. The T25 flask was taken out of the incubator, and first inspected using a microscope. Most of the cells adhered to the surface of the flask. The cells moving with the fluid were dead cells, and therefore, they were removed.

To change the medium and remove the debris, the T25 flask was opened in the fume hood and tilted so that all the medium was collected at the bottom corner of the flask. The medium was slowly drawn out using a pipette. 1-2 mL PBS was added and slowly swiped over the surface of the flask and then again drawn out in the same manner. Then, 10 mL of new growth medium was added to the flask. The T25 flask was then sealed, and checked under the microscope. After confirmation of the presence of the cells, the flask was again placed in the incubator at the same temperature and CO^2 level.

After 48-72 hours, the T25 flask was examined for cell growth under the microscope. If the cells covered more than 85% of the surface, the cells had to be transferred to a bigger flask, the T75 flask. The transfer of the cells is called passage. To pass the cells to the T75 flask, the medium was removed from the T25 flask. 2-3 mL PBS was added, the surface was rinsed, and PBS was removed. After this, 1-2 mL trypsin EDTA enzyme was added to the flask. The T25 flask was then incubated for 2 min. This enzyme helps the cells detach from the surface of the flask.

27

After the incubation time of 2 minutes, the flask was opened in the fume hood, and 8-9 mL of growth medium was added. The total volume in the flask was 10 mL including the trypsin EDTA. The surface of the flask was rinsed 3-4 times using the same medium inside the flask. Then, the medium was transferred from the T25 flask to a 15 mL falcon tube, and it was centrifuged at 1000 rpm, for 5 min. Meanwhile, the T75 flask was prepared. The name, cell line name, date, and passage number were written on its sides. The passage number was one plus the previous flasks passage number. Once the centrifuge was done, the medium was carefully removed from the tube, and 10 mL growth medium was added to the tube. The tube was rinsed from the bottom in order for the cells to start floating in the medium. Once the cells were floating, 1 mL of this medium with cells was transferred to the T75 flask. Furthermore, 19 mL of growth medium was added to the T75 flask to make up 20 mL of total volume. The T75 flask was sealed and observed under the microscope. The cells were visible, so the T75 flask was incubated at 37°C.

After 48 hours, the medium was changed using the same procedure, and the cells were again incubated until they covered about 85% of the surface of T75 flask. The cells had to be seeded on a 96 well plate. The medium was removed, cells were rinsed in PBS, trypsin EDTA was added to take off the cells from the surface, and after adding the medium, the cells were centrifuged. After centrifuge, 1 mL of the cells was transferred to a new T75 flask with passage number with an increment of one.

From the remaining 9 mL of the cell solution, cells were to be seeded on the well plate. Before that, a Neubauer hemocytometer (Celeromics) was used for cell counting. 100 μL cell solution was taken and diluted 50% by addition of 100 L trypan blue solution. The trypan blue solution is a blue color dye that helps living cells be more visible, and hence, they are counted with ease. After mixing the solution of dye with cells, 10 μL of the solution was placed on the hemocytometer with the lid on top. Once the solution filled the area, the hemocytometer was placed under a microscope.

The cells were counted from the 4 corners of the hemocytometer, and an average number of the cells was taken. The average was then multiplied by the dilution factor, 2 in this case, and by the surface area of one block of the hemocytometer (10,000). This gave the total number of cells in 1 mL. After calculations, 19.4 μL of the cell solution, with a density of $2.0 * 10^4$ per well, was transferred to each well with addition of 280.6 μL growth medium. The well plate was incubated at 37°C, and the cells were allowed to adhere to the wells.

3.2.5.2 Cell viability assay

After 24 hours, in a separate 96 well plate, FBS free growth medium was added with addition of BCD, MCD, IC, and MIC, each at concentrations of 1.0 mg/mL, 0.5 mg/mL, and 0.1 mg/mL. These samples were prepared in 1 X PBS at the above stated concentrations. Additionally, PFH concentrations of 0.1 μL, 0.12 μL, and 0.15 μL were added to a separate set of FBS free medium. This medium was selected because FBS contains different proteins, and thus, it might interact with the samples. The total volume of the medium and sample solution was adjusted to be 200 μL. Then, the medium from above the cells was replaced by the FBS free medium plus the sample solutions. The well plate was then incubated at 37°C for 24 hours. Afterwards, the medium from the well plate was removed, and 100 μL medium was added with addition of 10 μL CellTiter 96$^{®}$ Aqueous One Solution Cell Proliferation Assay (MTS assay). The well plate was then incubated at 37°C for 2 hours. After incubation, the well plate was read using the well plate reader at an absorbance of 490 nm.

The percentage of cell viability was calculated according to the following equation:

$$\% Cell\ viability = \frac{Absorbance\ of\ sample - absorbance\ of\ negative\ control}{Absorbance\ of\ positive\ control} * 100\%$$

(3.2)

where negative control contains only the cells with medium, and positive control

29

contains cells with medium and dye.

3.2.6 Fluorescence probe method (Investigation of critical micelle concentration)

To see if the MIC is forming self-assembly or not, a critical micelle concentration test was conducted. This was done using the fluorescence probe method followed by Alkayal et al. [104]. Briefly, a pyrene solution (1.0 X 10-4 mmol/mL) in acetone was prepared. 0.1 mL of this solution was added to different vials, and acetone was evaporated in the air. After complete evaporation, MIC solutions were prepared in PBS, at concentration of 1.0 mg/mL, 0.5 mg/mL, 0.1 mg/mL, 0.01 mg/mL, and 0.001 mg/mL each, were added to these vials. The total volume of each vial was adjusted to be 1.0 mL. These solutions were vortexed for 5 minutes, followed by 10 minutes of sonication. 200 μL of these solutions were transferred to 96 well plate. The emission spectrum was recorded using spectra max at ex = 337 nm, and the emission bandwidth was selected to be 5.0 nm.

3.2.7 Ablation of agarose tissue phantom using inclusion complex as a histotripsy agent

To test the MIC histotripsy agent, agarose phantoms were chosen as a medium. This was because the agarose phantoms provided a well-controlled viscoelastic medium, which was very important for the study as the damage in the tissue is induced by the histotripsy highly depends on the mechanical properties of the tissue [20]. The phantom was made using 1% agarose w/v by slowly mixing agarose powder (Agarose type VII, Sigma Aldrich) into saline solution. The temperature of the solution was raised above 70°C until the solution became completely transparent. The solution was then degassed using a partial pressure vacuum of 2.7 KPa for 30 minutes. The agarose solution was then cooled down to 37°C.

To achieve phantoms containing MIC, and only PFH, as a positive control, the MIC and pFH was slowly added to different gel solutions at around 40°C while the solution was still stirring and being colled down. The agarose mixture was then poured into rectangular molds make of polycarbonate, and placed at 4°C. The solutions were allowed to solidify, and the tissue phantoms embedded with MIC (test), with PFH (positive control), and without MIC (negative control) were obtained.

Two different histotripsy probes were used to perform two different experiment. In the first experiment, a 500 kHz transducer was used, and single cycle per pulse was transmitted at voltages of 30 V and 40 V. 40 V voltage corresponded to the maximum pressure used for histotripsy, without any use of the agents. 30 V voltage corresponded to the pressure lower than that threshold pressure. If the MIC worked at lower voltages, that means that it is working properly just like the nanodroplets. The cavitation behavior of the MIC was observed using a high-speed optical camera (V210, Vision research, Wayne). After every pulse, the camera captured images of the focal zone in the phantom. The camera was focused using a macro-bellows lens (Tominon, Kyocera) which was attached to the optical window of the chamber to observe the focal region. A light source was used at the back of the phantom, continuously, to produce shadowgraphic images of the cavitation bubbles.

3.3   Characterization

3.3.1   Hydrogen nuclear magnetic resonance spectroscopy

Once the IC and MIC were synthesized, a hydrogen nuclear magnetic resonance spectroscopy (^{1}H NMR) was performed for the confirmation of the complex formation. For this purpose, MCD, IC and MIC were observed through Agilent VNMRS 500 MHz nuclear magnetic resonance spectrometer. A chemical peak shift was compared between BCD and MIC for the methylation, and between

MCD and MIC for the formation of MIC.

3.3.2 Fluorine nuclear magnetic resonance spectroscopy

For further confirmation of the synthesis of the complex, Agilent VNMRS 500 MHz nuclear magnetic resonance spectrometer was used to carry out the Fluorine nuclear magnetic resonance spectroscopy (^{19}F NMR). MIC, and PFH were inspected, and the results were compared.

3.3.3 Fourier transform infrared spectroscopy

A Fourier transform infrared spectroscopy (FTIR) was carried out using the Agilent Cary 630 FTIR spectrometer. FTIR of CD, MCD, IC, MIC, and PFH were performed using a diamond crystal, with range of 4000 cm^{-1} to 400 cm^{-1}, resolution of 4 cm^{-1}, and 16 scans per minute. The peak shifts were observed and compared to each other to confirm the synthesis of the complex.

3.3.4 Thermal gravimetric analysis

To see and compare the weight loss profiles of BCD, MCD, and MIC, they were tested through thermal gravimetric analysis (TGA) using EXSTAR TG/DTA 7300. The weight loss was measured as a function of temperature. The heat flow was 10°C/min, from 25°C-700°C, under nitrogen flow. The results were compared to see the degradation of each sample, and also the stability of each compound.

3.3.5 Gas chromatography

Gas chromatography (GC) was performed as a part of the quantitative analysis to calculate the efficiency of the complexes. In other words, the amount of PFH

entrapped in the CD or MCD was calculated. Agilent Technologies 7820A GC System was used to perform this analysis. To calculate the amount of PFH present, first a calibration curve was formed using DMF as the solvent, anisole as internal standard and PFH. Initially, PFH, DMF, and anisole were injected in the GC individually. This was done to see the time at which the peak of each of the substance comes out. As the amount of PFH was very small in the samples (in μL range), it was impossible to compare it with the peak of DMF, as 200 mL of DMF was used. Thus, there was a need for an internal standard, whose peak should not overlap with either DMF or PFH. Anisole was a perfect match for this condition.

For the preparation of the calibration curve, in a 200 mL volume of DMF, 2 μL of anisole was added. This was the standard solution for the calibration curve, and also for the samples to be tested. The PFH amount was varied for each run, starting from 0.1 μL to 1.0 μL. This range was chosen because it corresponds to the range of the amount of PFH in a sample of 10 mg which was to be tested. A 6-point calibration curve was constructed.

After collecting the data, the six points were plotted on a graph and a line of best fit was constructed. Furthermore, the equation of the line of best fit was used to calculate the amount of PFH present in the sample. Following is the equation of the calibration curve, which was used to find out the volume of PFH.

$$A = 1.0273(V) + 0.0005 \tag{3.3}$$

Where A is the area of the PFH curve with reference to anisole and V is the volume of the PFH.

10 mg of IC and MIC, each with different ratios of PFH, were tested, and the peak areas were compared with anisole. The areas were then matched with the calibration curve to find out the amount of PFH present. The percentage efficiency of the complex was calculated accordingly. Each run for calibration curve and sample was tested for a temperature range of 40°C 200°C, at a heating

rate of 40°C/min, and the sample was kept at 200°C for one minute.

When the volume was calculated from this equation, the percentage of PFH present in the complex was calculated according to the following equation.

$$\%PFH = \frac{V}{U} * 100\% \qquad (3.4)$$

Where V is the volume of PFH in the sample calculated from the previous equation, and U is the theoretical volume at 100% encapsulation of PFH in the CD and MCD. The efficiencies of IC and MIC were compared based on the results of GC calculated using the calibration curve.

3.3.6 Dynamic light scaterring

Malvern Zetasizer Nano ZSP was used to calculate the dynamic light scattering (DLS) measurements. Solutions of CD, MCD, IC, and MIC were prepared in 1 X PBS. Each measurement was calculated using 3 runs, and each run contained 12—16 repetitions. The sizes of CD, MCD, IC, and MIC were calculated as an average of the sum of all the values, and the results were compared.

3.3.7 Scanning electron microscopy

To see the textural changes on the samples and how they differ form each other at nano level, BCD, MCD IC, MIC were observed in a scanning electron microscope (SEM, Philips XL 30S FEG with EDAX detector). Images of different samples were taken. Also, freeze dried samples of MIC at concentration of 1.0 mg/mL and 0.1 mg/mL in water and PBS were observed to see whether there is self-assembly formation or aggregation at higher concentrations. The samples were also checked for % fluorine content using the Energy dispersive x-ray spectroscopy (EDAX) detector in the SEM.

Chapter 4

Results and discussions

A histotripsy agent consisting of BCD and PFH was aimed to be synthesized using a host-guest chemistry. PFH is a small hydrophobic chain of six carbon atoms, all containing fluorine atoms attached to them. Because of its highly hydrophobic behavior, it is challenging to deliver it to the human body. Thus, the host guest chemistry is used, which is a perfect solution for carrying such hydrophobic molecules into the body. BCD, which is comprised of seven sugar chains, has a cone like structure. The exclusive feature of BCD, apart from being biocompatible, is that it has a hydrophilic outer surface with a hydrophobic inner cavity. BCD acts as a host and offers a place for hydrophobic guest molecules to fill the cavity. In our case, PFH acts as the guest molecule and fills the cavity of the BCD hence forming an IC. Figure 4.1 one depicts a visualization of the process of host-guest chemistry and shows the filled cavity.
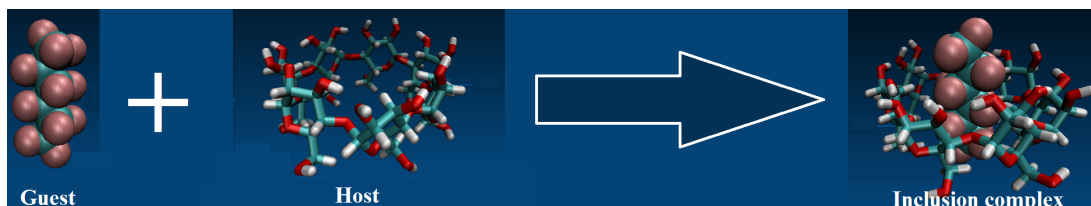

Figure 4.1: Visual representation of the formation of an IC

4.1 Preparation of inclusion complex

The IC was produced using BCD and PFH. First BCD was dissolved in water at 80°C and cooled down to 45°C. Upon achieving this temperature, PFH was added in different molar ratios. The molar ratios used were (BCD: PFH) 1:1, 1:5, 1:20, and 1:50. It was observed that due to the lower solubility of BCD in water at room temperature (18.5 mg/mL), when the temperature of the solution went below 60°C, white precipitates of BCD started to appear. As the temperature went lower, until 45°C, the solution became more heterogeneous.

The percentage (%) yield for the reaction was calculated by weighing the material before and after the reaction. For the ratios of 1:1, 1:5, 1:20, and 1:50, the % yield was 57% ± 2%, 60% ± 3%, 62% ± 7%, and 65% ± 3%, respectively. The % yield is listed in the Table 4.1 for each of the ratios tested. Furthermore, the encapsulation efficiency (EE) of the IC was calculated using GC. For the EE calculations, first a calibration curve was constructed using known concentration of PFH in the solvent system, DMF ($200\mu L$) + anisole ($2\mu L$). This solvent system was chosen because their peaks did not overlap with each other and with that of the PFH. The peak of PFH was seen at 0.675 min, whereas the peaks of DMF and anisole were seen at 2.14 min and 2.45 min, respectively. Anisole was intended to be used as an internal reference. Thus, 2 μL of anisole was used in each solvent so that the resulting area of PFH peak can be compared to the anisole peak.

For the calibration curve, six different concentrations of PFH were used which were 1.0 μL, 0.2 μL, 0.25 L, 0.5 μL, 0.75 μL, and 1.0 μL. As the maximum amount of encapsulation could be 1.36 μL, thus, this range was optimum for the calibration curve. The area of PFH at these known concentration were compared with area of anisole, which was kept at a fixed concentration in each run. The calibration curve was then used to calculate the volume of PFH present in the samples based on the area calculated using the same solvent system. Figure 4.2 shows the resulting calibration curve and also shows a small-scale GC thermogram for the solvent system used.
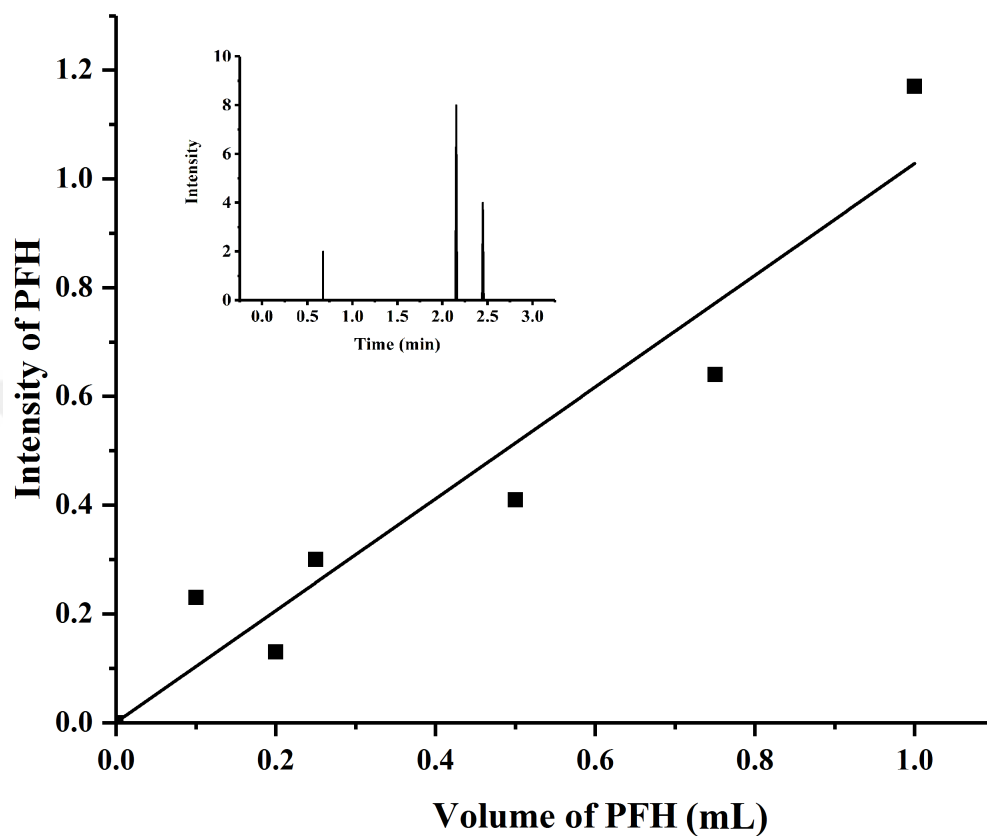
Figure 4.2: The calibration curve made using GC for the quantitative analysis of amount of PFH in IC and MIC.

For each sample, the EE was different and varied a lot from each other. Table 4.1 lists the values of EE and % yield. For 1:1, 1:5, 1:20, and 1:50, the EE which was calculated turned out to be 67.5% $\pm$ 9%, 31.0% $\pm$ 7%, 26.9% $\pm$ 1.8%, and 88.8% $\pm$ 21%, respectively.

Table 4.1: % yield and EE of different ICs produced using different molar ratios.

Molar ratio (BCD:PFH)	Percentage yield	Encapsulation efficiency
1:1	57% ± 2%	67.5% ± 9%
1:5	60% ± 3%	31.0% ± 7%
1:20	62% ± 7%	26.9% ± 2%
1:50	65% ± 3%	88.8% ± 21%

It was observed that the IC with 1:50 (BCD: PFH) gave the highest EE of PFH present in BCD but was not consistent. It was anticipated that this fluctuations and inconsistency in the results of EE might be because of the low solubility of BCD. As at the time of addition, the solution already heterogeneous, and part of the BCD dissolved in water was already precipitated. Hence, there was a lower amount of dissolved BCD, providing less number of cavities present to accommodate the PFH present in the solution.

Thus, to verify the above hypothesis, the solubility of BCD was increased by random methylation of BCD. Methylation of BCD is a common procedure in the literature to increase the solubility of BCD [103, 105, 106]. Furthermore, with the addition of small methyl groups, the properties of CD will almost remain the same. Hence, the BCD was randomly methylated using DMC and a methylation degree between 60% - 80% was aimed. For this purpose, BCD was dissolved in DMF, and K_2CO_3 and DMC were added drop-wise. After the reaction, the ^{1}H NMR of MCD was analyzed and compared with that of the BCD. The comparison of both the ^{1}H NMR is given in Figure 4.3, where a clear peak shift can be seen.

In the ^{1}H NMR spectrum of BCD it can be seen that there are visible peaks of —OH, labeled a, b, and c. The integrated area of these three peaks were 1.0 if compared with the area of the H peak labeled as 1. After the methylation of BCD, the —OH peaks diminished and the intensities of all three peaks of —OH were lowered. Integrating thee peaks and comparing them with integrated area of 1 gave us values of 0.26, 0.26, and 0.17 for a, b, and c, respectively. By taking an average of these three values, we get an area of 0.23 compared to 1. This reveals that the total methylation was around 77%.
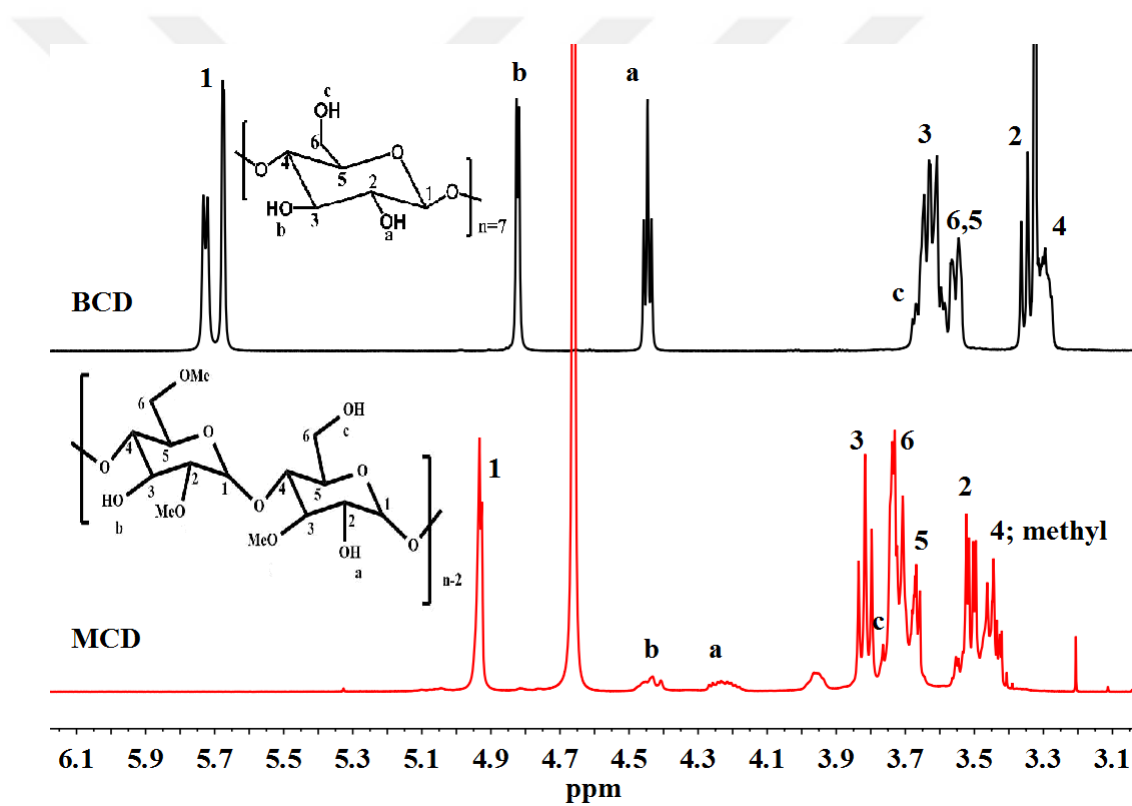
Figure 4.3: ^{1}H NMR spectrum of BCD and MCD. A clear peak shift and a decrease in the intensities of a, b, and c can be seen.
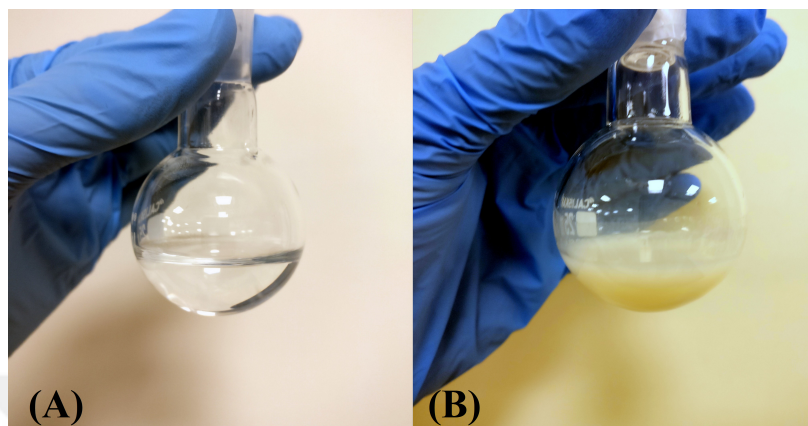
Figure 4.4: Comparison of reaction flask before and after addition of PFH at room temperature. There is a clear visual difference in the solution color proving the formation of the MIC.

After methylation, the solubility of MCD increased eminently. The initial procedure of the synthesis of the complex was repeated, using MCD instead of BCD. 50 mg of MCD was readily dissolved in water at room temperature in three different vials. PFH at molar ratios of MCD: PFH 1:2, 1:5 and 1:10 were then inserted to the solutions. Since the solubility of MCD was enhanced, smaller molar ratios of PFH were tried. Just after a few minutes of addition of PFH, the solution started to turn white and precipitates of the product were seen. Since the MCD was completely soluble, and the solution was clear, this occurrence of the precipitates was an indicator that the reaction is moving forward and the MIC was being formed. Figure 4.4 compares two pictures of the round bottom flask in which the reaction took place. On the left, it shows the flask which contains a clear solution of MCD. On the right, there is a picture of the same solution after the addition of PFH. It can be clearly seen that after the addition of PFH, clear precipitates of MIC were seen and the solution turned to a white heterogeneous solution.

The % yield was calculated by weighing the product after reaction was completed. The % yield found out to be 40% ± 3%, 71% ± 7%, and 68% ± 4%, for the molar ratios of MCD: PFH 1:2, 1:5, and 1:10, respectively. There was a slight increase in the % yield of the MIC compared to the IC. Moreover, the EE was calculated for the MIC using the same calibration curve using GC and the

interesting results were listed in Table 4.2. For the molar ratios of MCD: PFH, 1:2, 1:5, and 1:10, the EE revealed to be 97% ± 2%, 98% ± 3%, and 130% ± 3%, respectively.

Table 4.2: List of % yield and EE of different MICs produced using different molar ratios.

Molar ratio (MCD:PFH)	Percentage yield	Encapsulation efficiency
1:2	40% ± 3%	97% ± 2%
1:5	71% ± 7%	98% ± 3%
1:10	68% ± 4%	130% ± 4%

The result for the EE of 1:10 MIC was unique and provided us with new ways to picture the formation of the complex. Previously, it was expected that one PFH chain can enter the cavity of the CD or MCD, but the EE calculation for 1:10 MCD: PFH portrayed new assembly scenario for the complex. As the EE calculations were based on the illustration that one PFH can enter one cavity, 100% EE depicted that all of the cavities were filled with one PFH. Since the EE of 1:10, MCD: PFH, came out to be more than 100%, it provided evidence that there might be a possibility of two PFH fitting in one cavity. Figure 4.5 illustrates two different scenarios, from top and side views, in which PFH can fill the cavity. This debate needs to be further addressed, and more experimentation needs to take place in order for more evidence to be provided.

Based on better results of MIC for % yield and its ability to form complex with absolute EE, it was decided to be used rather than IC. Therefore, BCD, MCD, and MIC were tested for most of the characterization techniques, for all of the cell toxicity experiments, and for the histotripsy experiment, while IC was neglected.
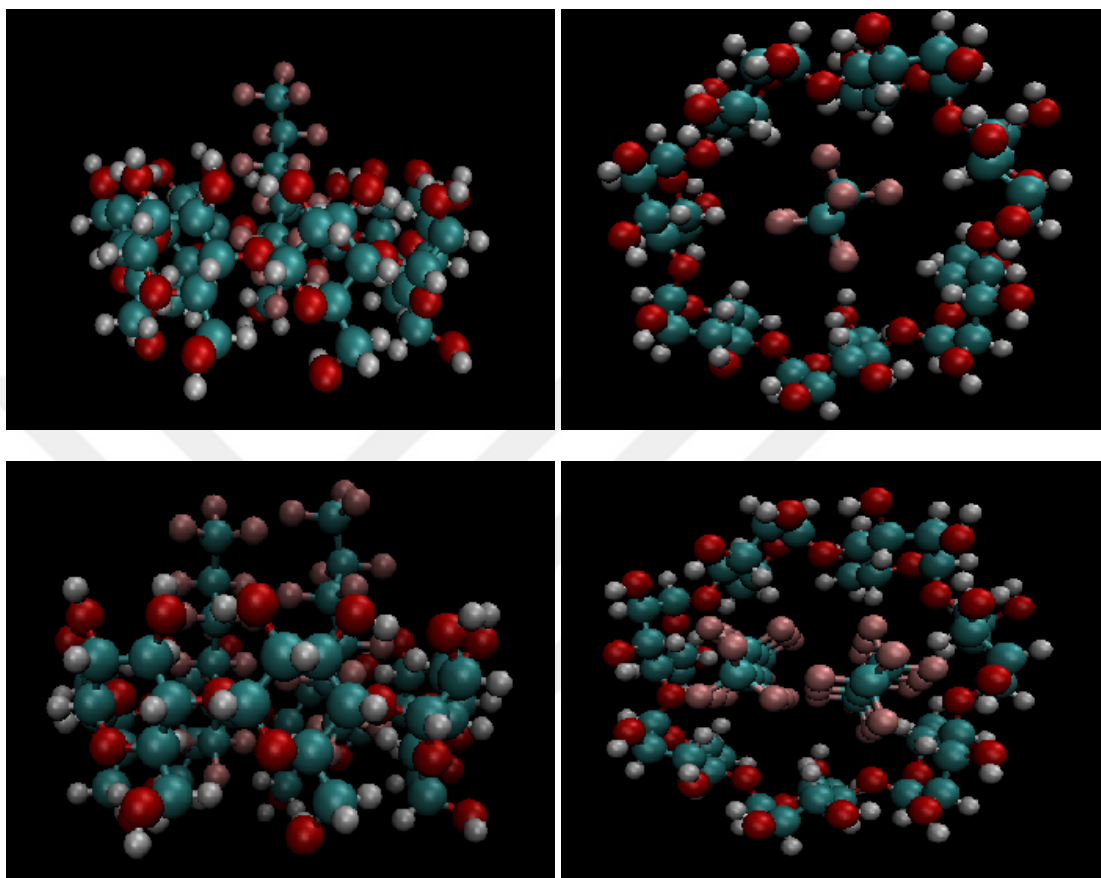
Figure 4.5: Picture on the left shows the prediction of one PFH filling the cavity of BCD or MCD(side and top view). On the right, the prediction of two PFH filling one cavity is shown (side and top view)

4.2 Characterizations of inclusion complex

4.2.1 Nuclear magtenic resonance spectroscopy

To confirm the formation of the complex, BCD, MCD and MIC were tested through ^{1}H NMR spectroscopy (Figure 4.6). Glucopyranose units of BCD has six protons on the carbons and 3 protons on hydroxyls protons whose peaks are visible in the ^{1}H NMR spectrum. The protons 1, 2, and 4 are present at the outer surface of the BCD. Protons 3 and 5 lies inside the cavity, and are most important to identify and study the formation of the complex. While, 6 is the sixth proton which is located at the minor border of the cavity of the BCD [107].

The formation of the MIC was first studied using the changes in the chemical shifts (δ) of the protons in the MIC compared to MCD. Table 4.3 lists the peak assignments of BCD, MCD, and MIC, and their chemical shift deviations due to the formation of the complex.

Figure 4.6: ^{1}H NMR spectrum of MCD and MIC recorded in D$_2$O and DMSO, respectively.

Table 4.3: Peak assignments for ^{1}H NMR spectrum of MCD and MIC and their change in ppm

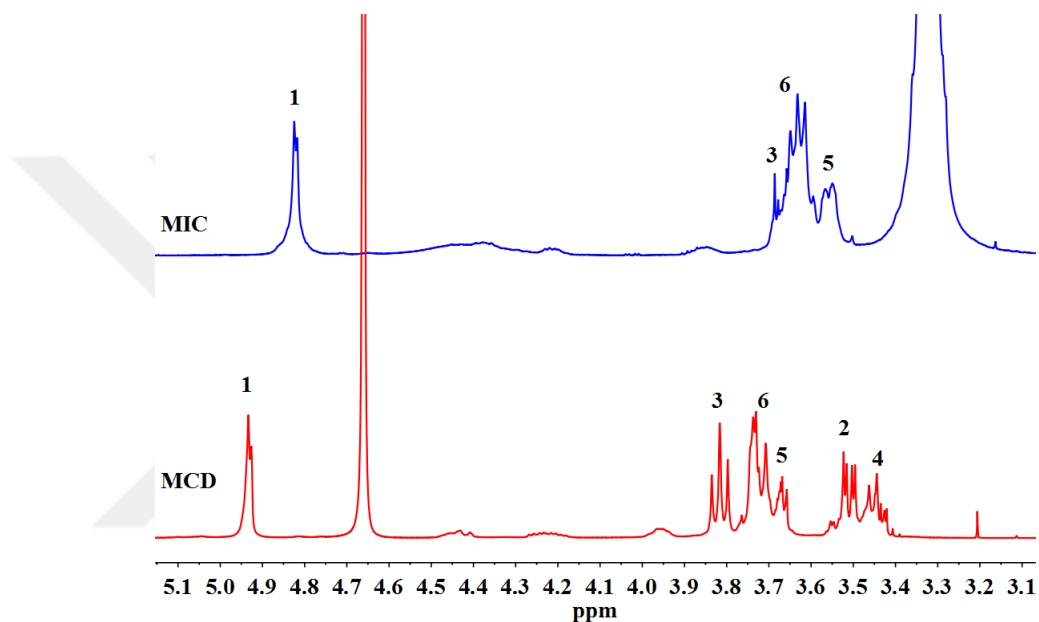| Assigned peaks	MCD (ppm)	MIC (ppm)	δ (ppm)
1	4.933	4.825	0.108
2	3.523	ND	ND
3	3.816	3.686	0.130
4	3.449	ND	ND
5	3.707	3.566	0.141
6	3.731	3.649	0.082
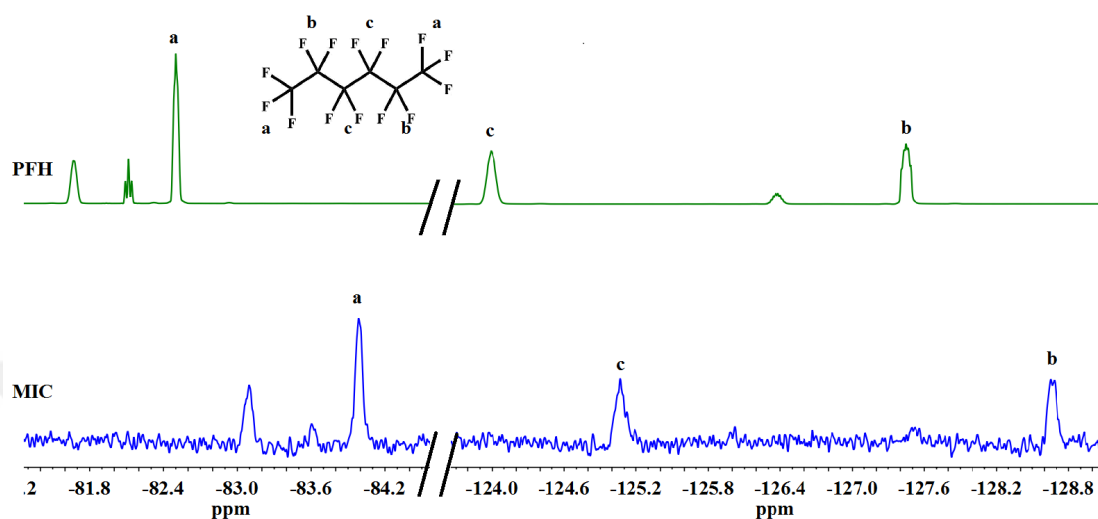
Figure 4.7: ^{19}F NMR spectrum of MIC and PFH. Clear shift of peaks of CF$_3$ and CF$_2$ can be seen.

Other than ^{1}H NMR, ^{19}F NMR was also performed to further confirm the presence of fluorine in MIC. Therefore, a ^{19}F NMR was performed for PFH and MIC in D$_2$O. First of all, the ^{19}F NMR spectrum of MIC showed peaks of fluorine (Figure 4.7) which confirms the development of the complex as MCD contains no fluorine atoms, while in the ^{19}F NMR spectrum, clear peaks of fluorine are seen. Furthermore, when compared with the ^{19}F NMR spectrum of PFH, a clear peak shift can be seen. Table 4.4 lists the δ ppm values for the peaks of CF$_3$ and CF$_2$, labeled as 'a', 'b', and 'c'.

Table 4.4: Peak assignments for ^{19}F NMR spectrum of PFH and MIC and their change in ppm

Assigned peaks	PFH (ppm)	MIC (ppm)	δ (ppm)
a (CF$_3$)	-82.501	-83.986	1.485
b (CF$_2$)	-127.447	-128.651	1.204
c (CF$_2$)	-123.993	-125.067	1.074

It can be seen from the Table 4.4 that the peak 'a', which represents CF$_3$, has the highest δ ppm value, followed by 'c' and then 'b'. This data correlates with the data of Gou et al. confirming the formation of the complex [108]. Also, a decrease along the ppm values of the peak were seen, which was also claimed by

the same researchers [108]. Thus, ^{19}F NMR studies provided enough evidence for the formation of the complex.

4.2.2 Fourier transform infrared spectroscopy

FTIR was performed to confirm the methylation of BCD and also the formulation of the MIC. The spectrum of BCD, MCD, PFH, and MIC are presented in Figure 4.8. The FTIR spectrum of BCD showed a characteristic peak at 3200-3400 cm^{-1} due to the O-H group stretching. The characteristic peak at 2854 cm^{-1} is seen due to C-H asymmetric/symmetric stretching. Additionally, a peak at 1650 cm^{-1} represented the H-O-H deformation bands of water present in BCD cavity. Peaks at 1153 and 1029 cm^{-1} indicated C-H overtone stretching and that at 1029 cm^{-1} C-H, C-O stretching. Absorption of the C-O-C vibration was seen at 1153 cm^{-1} [109].

Spectrum of MCD shows all the above characteristic peaks of BCD in addition with a broad peak of methyl group at 1383 cm^{-1}. Another peak appeared at 1745 cm^{-1} which was due to the carbonate impurities present during the methylation of the BCD.
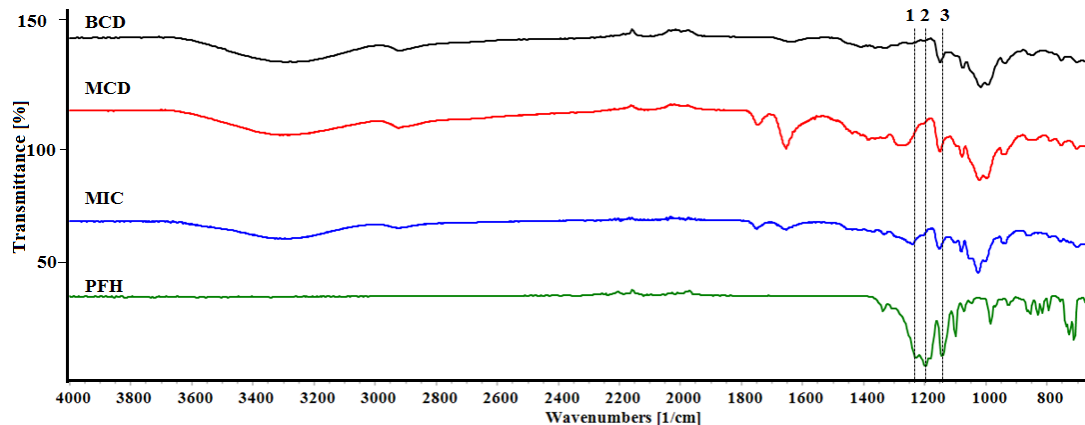

Figure 4.8: FTIR spectrum of BCD, MCD, PFH and MIC.

45

According to the literature, the characteristic peaks of CF_2 appears at 1230 cm $^{-1}$ and 1150 cm $^{-1}$, whereas the characteristic peak of CF_3 appears at 1210 cm $^{-1}$ [110, 111, 112, 113]. The same characteristic peaks were seen in the FTIR spectrum of PFH, and were labeled as 1, 2, and 3 (Figure 4.8). Although, the peak at 1150 cm^{-1} was overlapping with a peak of BCD and MCD, clear peaks can be seen at 1230 cm^{-1} and 1210 cm^{-1} in the spectrum of MIC, proving the presence of PFH in the cavity, hence providing evidence for the formation of the complex.

4.2.3 Thermal gravimetric analysis

TGA is considered to be a useful and adequate technique to investigate the physical and chemical properties of any substance when heating is applied [114]. Figure 4.9 shows the TGA thermograms of BCD, MCD and MIC. The thermogram of BCD revealed that mass loss occurs at two different stages. The first stage is the temperature ranges up to 110°C, where the weight loss observed is 9.55%. This loss was due to the loss of water from inside the cavity of the BCD. For the same region, the thermogram of MCD shows a weight loss of 7.68%, which is lower than that of the BCD. Finally, the MIC thermogram shows a higher decrease in the weight compared to BCD or MCD in the first stage. Also, the weight loss starts much earlier than that of MCD or BCD. In the same region of 25°C - 110°C, 19.25% weight loss was seen. This radical change can be explained because of the encapsulation of the cavity by PFH. Since PFH has a lower boiling point that water (56°C), a higher weight loss is seen.

Moreover, BCD was seen to be more stable than both MCD and MIC as it starts to degrade the latest. BCD started degrading at 300°C, while MCD and MIC started degrading at 200°C and 250°C, respectively.

To check the calculations of EE from GC, a calculation for the EE was also performed using the weight loss of MIC. It was seen that MIC lost around 19.5% of its initial mass, which was 2290.5 μg, at 200°C. this was calculated to be 446.7 μg. Moles of PFH were calculated using this mass, which turned out to be 1.32
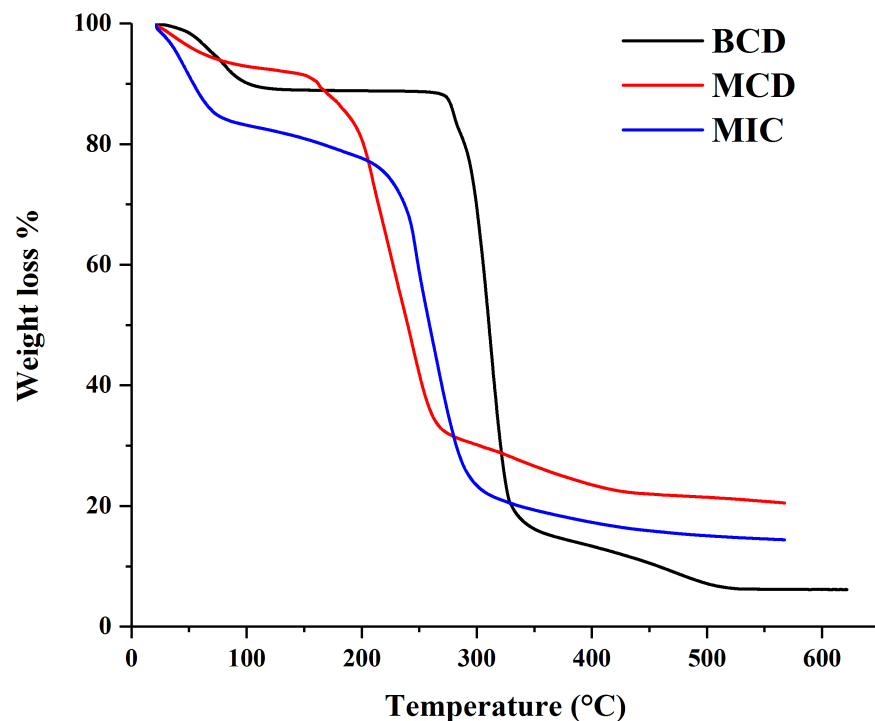
Figure 4.9: Thermal gravimetric analysis of BCD, MCD, and MIC.

x 10^{-6} mol. From the remaining material, which was 1843.8 μg, moles of MCD were calculated, which were 1.42 x 10^{-6}. The ratio of the moles of PFH and MCD were calculated and the result was 0.93, which means, according to these calculations, the EE of MIC was 93%, which supported our previous results form GC.

4.2.4 Dynamic light scattering

The size of the complex is a very important parameter as it effects the threshold of the histotripsy. Also, smaller size is favorable for injection, as smaller the particle, higher the chance of accumulation of the particles into the tumor. As it has been reported that the size of the leaky vasculature is starts from around 200 nm, therefore, the particles measuring lower than 200 nm are more efficient in

delivering drug, or accumulating in the tumor using the enhanced permeability and retention (EPR) effect [115].

Moreover, the average size of the nanodroplets was reported to be 204 nm [20]. Hence, making a histrotripsy agent which is lower in size and works as efficient as the nanodroplets was outstanding. For our experiment, the size of CD found out to be 16.42 nm $\pm$ 2 nm which was small enough to be used in the body. Particles as small as the above can be easily transported to the tumor based on the EPR effect. Figure 4.10 shows a comparison of the sizes of CD, MCD and MIC.

DLS revealed the size of MCD to be 19.55 nm $\pm$ 2 nm. The slight increase is due to the addition of the methyl groups of the surface of the CD. MIC showed the size of 48.68 nm $\pm$ 7 nm. Even though the size of the complex is higher than both CD and MCD, still it is small enough to be used in vivo. These results clearly show that the size of the MIC is much smaller than the size cutoff (200 nm) of the tumor vasculature [116].
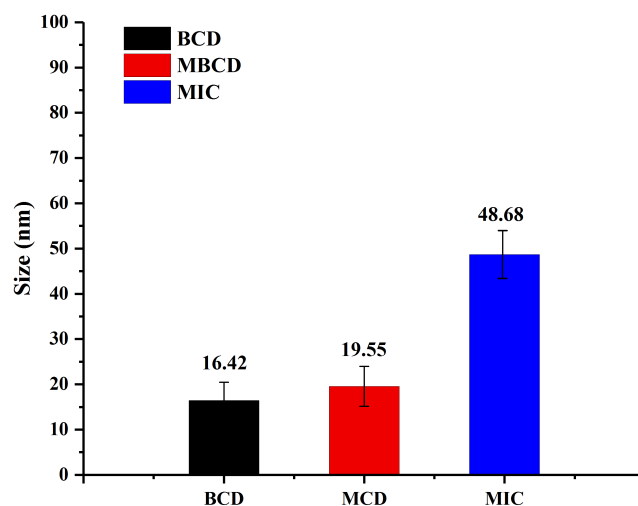
Figure 4.10: Size comparison of BCD, MCD, and MIC.

4.2.5   Scanning electron microscopy

SEM images of BCD, MCD, IC, and MIC were taken at different magnifications to see the changes on the morphology of the compound. Images at 5000X and 25000X magnifications are presented in Figure 4.12 for BCD, MCD, IC, and MIC. The structure of BCD was amorphous crystal which was changed, after methylation, to more rough crystals. A clear difference was seen in the images of inclusion complexes comparing to their precursor cyclodextrin derivatives indicating complex formation. Both IC and MIC showed smaller crystals, while MIC showed more plate like structure.

Furthermore, different MICs of 1:5 and 1:10 ratios were subjected to the EDAX detector and % fluorine was observed. It was revealed that the MIC with 1:10 contained almost 20% more fluorine content than MIC with 1:5. This result also supported our results from the GC. Figure 4.11 shows the images of the MIC at which the % fluorine was detected. Also, it contains the graph of EDAX and the percentage of carbon, oxygen and fluorine.

Figure 4.11: EDAX data showing % fluorine content in MIC 1:5 and 1:10.

Figure 4.12: Comparison of SEM images of BCD, MCD, IC, and MIC. (a)BCD at 5000X magnification. (b)BCD at 25000X magnification. (c)MCD at 5000X magnification. (d)MCD at 10000X magnification. (e)IC at 5000X magnification. (f)IC at 25000X magnification. (g)MIC at 5000X magnification. (h) MIC at 25000X magnification.

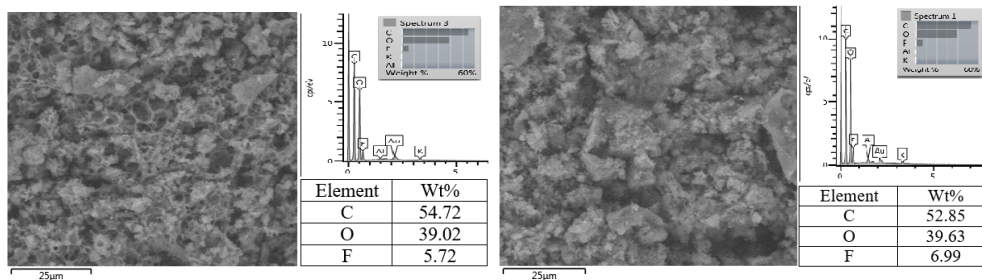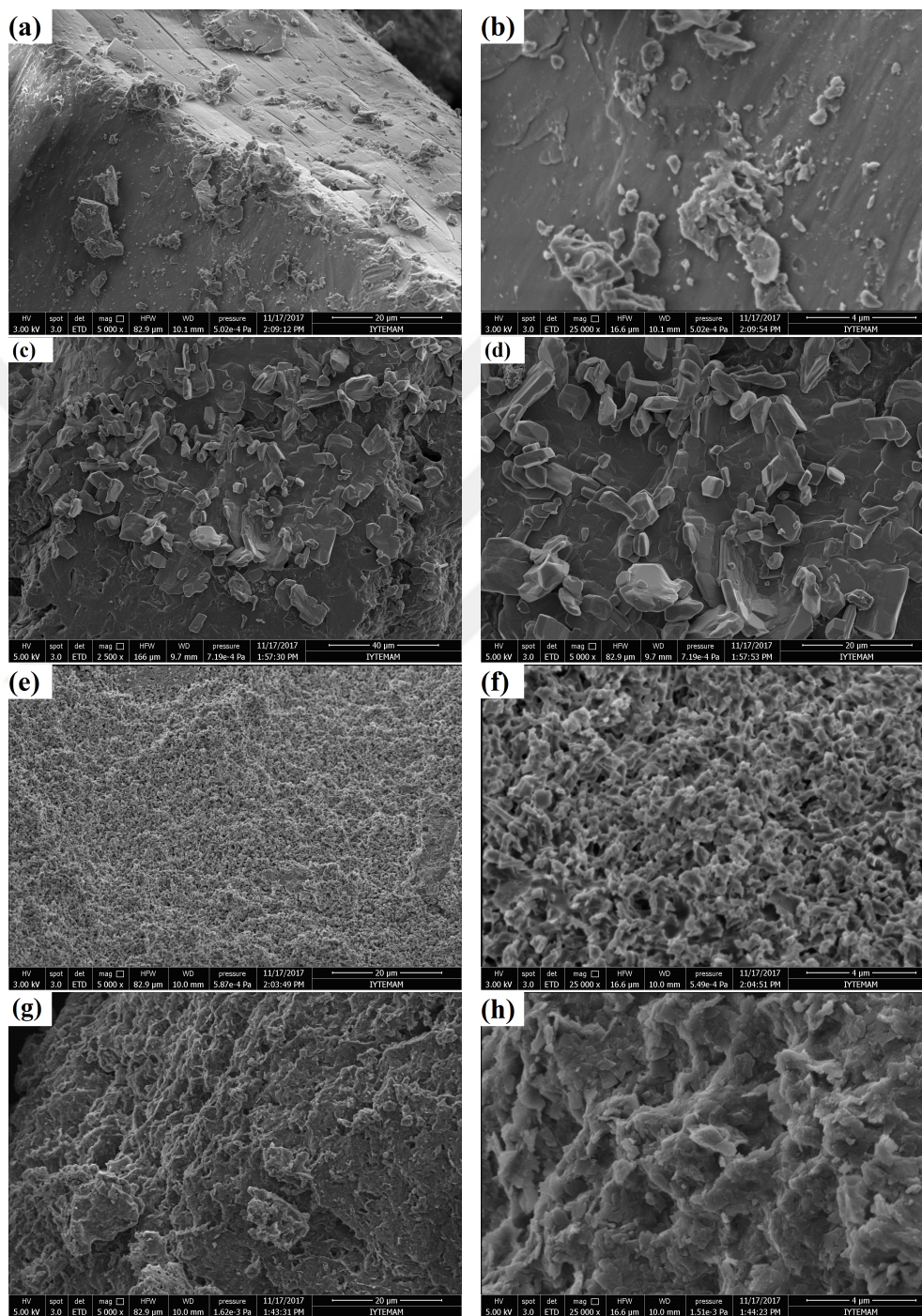## 4.3 Toxicity studies of the inclusion complex

4.3.1 Interaction with Red Blood Cells (hemolytic activity)

Since the complex relies on the blood circulation system after injection in the body, the interaction and toxicity index of the complex with RBCs is important. To examine the hemolytic level of the compounds, and their effect on the RBCs, different concentrations of BCD, MCD, and MIC were tested. Concentrations of 0.1 mg/mL, 0.5 mg/mL, and 1.0 mg/mL for BCD, MCD, and MIC were tested and the results are presented in Figure 4.13.

Satisfying results were achieved after the samples were read through the well plate reader. For concentrations of 0.1 mg/mL, 0.5 mg/mL and 1.0 mg/mL, BCD showed a hemolysis of 10.9% ± 0.45%, 9.5% 0.42%, and 4.8% ± 0.37%, respectively. MCD on the other hand revealed the hemolysis percentage to be 11.9% ± 0.46%, 9.6% ± 0.41%, and 16.1% ± 0.32% for the concentrations of 0.1 mg/mL, 0.5 mg/mL, and 1.0 mg/mL, respectively. The lowest hemolysis was caused by the MIC at each of these concentrations. At a concentration of 0.1 mg/mL, only 9.6% ± 0.43% hemolysis was caused. At 0.5 mg/mL and 1.0 mg/mL, hemolysis of 5.2% ± 0.34%, and 3.1% ± 0.34%, respectively, was recorded.

For MCD, the results came out to be as expected. There was a clear increase in the hemolysis of RBCs with the increased concentration of the MCD. As the concentration of MCD increases, the number of methyl groups on the outer surface of the BCD increases. Because these methyl groups may interact more towards the cell membrane, thus, they end up being more destructive towards the RBCs. It is because of this increase of methyl groups in increasing concentrations of MCD, an increase in the hemolytic level of MCD was seen.

The decrease in percentage hemolysis of BCD and MIC was surprising but it can be explained by the formation of self-assembly or by forming aggregates.
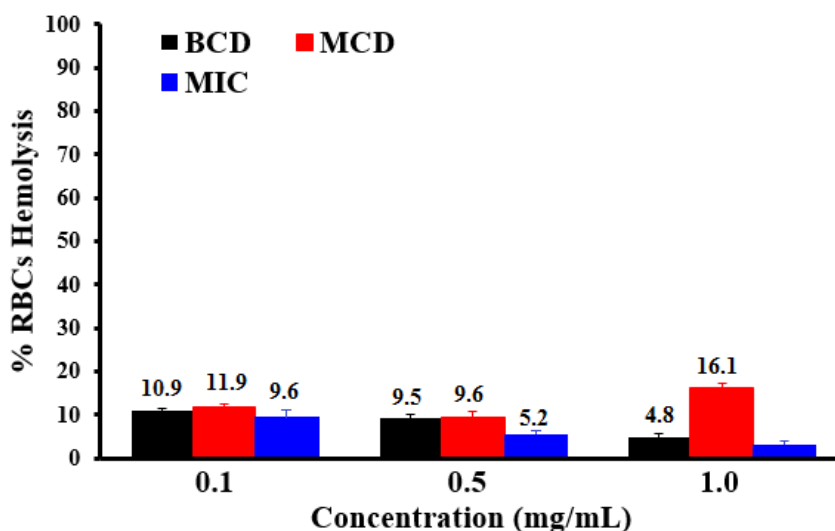
Figure 4.13: A representation of percentage hemolysis caused by BCD, MCD, and MIC.

For BCD, when the concentration is increased, the self-assembly or aggregates are formed, the overall particle concentration is decreased, hence less number of BCD particles interacts with the RBCs, resulting in a lower hemolysis percentage.

For MIC, two phenomenons might be going on in lowering the hemolytic level. Apart from one of the reasons explained above, another reason for a lower level of hemolytic activity at increased concentrations of MIC could be because of the formation of self-assembly or aggregates to lower the hydrophobic interaction between the cells and MIC. This happens by gathering all the hydrophobic part inside, and revealing only the hydrophilic part to the cells. Due to these reason, with an increase in the concentration of the MIC, the percentage hemolysis is decreases. To test the phenomenon of formation of self-assembly or aggregates, a DLS study, SEM imaging and a fluorescence probe experiment was performed.

The DLS studies were carried out at higher concentrations to see the size of the agglomerated or the self-assembled particles. The size for BCD at concentrations of 1.0 mg/mL, 0.5 mg/mL, and 0.1 mg/mL was found out to be 345 nm, 350 nm, and 211 nm. For MCD, the size was 319 nm, 224 nm and 103 nm for concentration

of 1.0 mg/mL, 0.5 mg/mL, and 0.1 mg/mL. The size of MIC at 1.0 mg/mL was 550 nm, at 0.5 mg/mL was 472 nm, and at 0.1 mg/mL the size was 48.68 nm.

Usually, concentrations up to 100μg/mL are tested for drug delivery [117, 76]. Based on this scale of calculations, the concentrations of 100 μg/mL, 500 μg/mL, and 1000 μg/mL were tested for BCD, MCD, and MIC. The results were still positive, proving that the concentrations as high as 1000μg/mL did not cause any harm to the RBCs, then the lower concentrations will also have no harmful effect.

4.3.2 Cell viability

The cell toxicity was an important parameter to see how MIC reacts with the cells in the body. Therefore, as a reticuloendothelial system (RES) organ, kindey cells, HEK-293T, were selected. The function of the RES organs is to clean up the blood and remove any particles or soluble antigens from the blood stream. Also, it is responsible for the generation of different inflammatory mediators based on the response of immunogenic stimulation. The aim was to investigate the interaction of the complex with these cells and examine the effect, since in body, these very cells will be responsible for cleaning out the complex.

For this purpose, similar concentrations of 0.1 mg/mL, 0.5 mg/mL, and 1.0 mg/mL were tested for BCD, MCD and MIC. The investigation of cell viability of PFH was critical, since it contains hydrophobic alkyl chains and has a potential to be toxic. For PFH, 0.1 μL, 0.13 μL, and 0.15 μL were tested. This was calculated based on the amount of PFH present in 1.0 mg/mL, which came out to be 0.15 μL. For 0.5 mg/mL and 0.1 mg/mL, the volume of PFH calculated was 0.075 μL and 0.015 μL. Such small volumes of PFH were inconceivable, thus volumes of 0.13 μL and 0.1 μL were tested, which were still higher than the calculated amount.
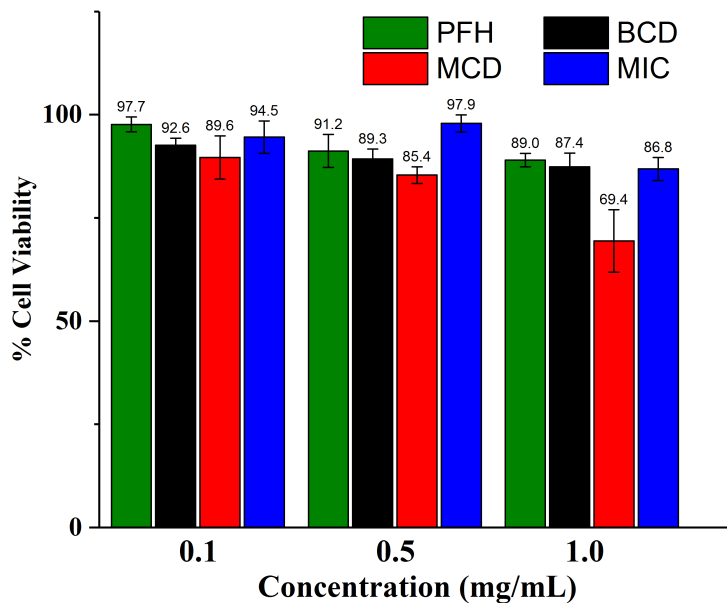
Figure 4.14: Cell viability of HEK-293T cells after incubation with different concentrations of BCD, MCD, MIC, and PFH.

Figure 4.14 displays the detailed results of the cell viability of each materials at different concentrations. It was revealed that upon incubation of the cells with MIC, the cells were more viable than any other compound (Figure 4.14. For concentrations of 0.1 mg/mL, MIC showed 94.5% cell viability, were as BCD and MCD showed 92.6% and 89.6%, respectively. The results were similar for 0.5 mg/mL as it showed 89.3% cell viability for BCD, 85.4% for MCD, and 97.9% for MIC. For 1.0 mg/ml, the cell viability of BCD and MIC was comparable as 87.4% and 86.8% cell were viable. MCD showed a significant decrease in the cell viability at 1.0 mg/mL, which was calculated to be 69.4%, which was consistent with the results of hemolysis. PFH on the other hand showed the cell viability of 97.7%, 91.2%, and 89.0% at 0.1 μL, 0.13 μL, and 0.15 μL, respectively.

4.4   Critical micelle concentration

Based on the results of hemolysis and cell toxicity, it was mandatory to check if the self-assembly is formed at higher concentrations because lesser toxicity was shown at higher concentrations of MIC. This could be possible by either aggregation or by self-assembly formation, by which all the hydrophobic parts interacts and combines together to form a new organization, exposing only the hydrophilic parts to the outer surface.

To confirm the self-assembly formation, concentrations of 0.001 mg/mL, 0.01 mg/mL, 0.1 mg/mL, 0.5 mg/mL, and 1.0 mg/mL for MIC were tested which uses pyrene as a fluorescence probe. The method works in a way that a very small amount of pyrene is added in the solutions of different concentrations. If the self-assembly is formed, pyrene will be trapped inside the self-assembly, and at a specific wavelength, the hydrophobic part of the structure would give reading as the fluorescence absorption becomes possible. If there is no self-assembly, there will be no detectable pyrene emission, since pyrene will be in water environment as insoluble fluorescence probe.

Based on the results of the emission intensities from the well plate reader, a graph of the intensities was constructed as a function of the concentration of the MIC. For this purpose, highest intensity coordinate was taken from each concentration of MIC. The points were scattered on a graph and a best fit curve was then drawn based on those points. After that, two tangents were then created at two different points on the best fit curve, one at a lower concentration and the other one at a higher concentration. The point of intersection of these tangents revealed the critical micelle concentration. According to the graph, the critical micelle concentration of MIC was calculated to be 0.295 mg/mL. This tells us that there will be no self-assembly below the concentrations of 0.295 mg/mL. For concentrations of 0.295 mg/mL and above, there will be a self-assembly. Figure 4.15 shows the graph with the scatter points, the best fit curve, the two tangents, and the critical micelle concentration point.
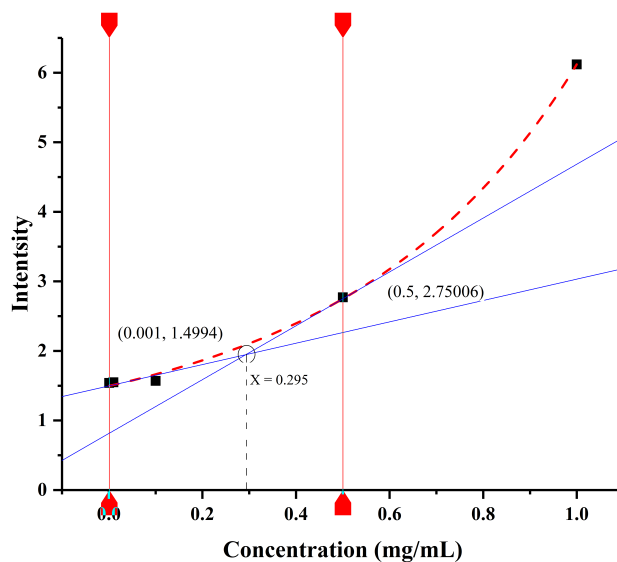
Figure 4.15: Fluorescence intensity of pyrene mixed with the different concentration of MIC. The two tangents cut at 0.295 mg/mL concentration which reveals the CMC for the MIC

4.5 Scanning electron microscopy of MIC at 0.1 mg/mL and 1.0 mg/mL concentrations

MIC solutions at concentrations of 0.1 mg/mL and 1.0 mg/mL were prepared and freeze dried. The resulting dry sample was subjected to SEM imaging to see if the organization of the particles were due to self-assembly formation or aggregation. The image captured at 0.1 mg/mL concentration showed PBS crystals with few MIC on it since it has low concentration compared to PBS salt. Once, MIC concentration was increased to 1 mg/mL, some aggregates were observed with a different pattern than PBS crystals. This was interpreted as either ionic interaction in PBS can cause aggregation of MIC, or different formation of PBS salt crystals can exist. No such aggregation was seen in samples of MIC dispersed in water.Figure 4.16 shows higher and lower magnification images of SEM of these samples at both concentrations in water and PBS. Hence, it was concluded that if a MIC is well dispersed in water.
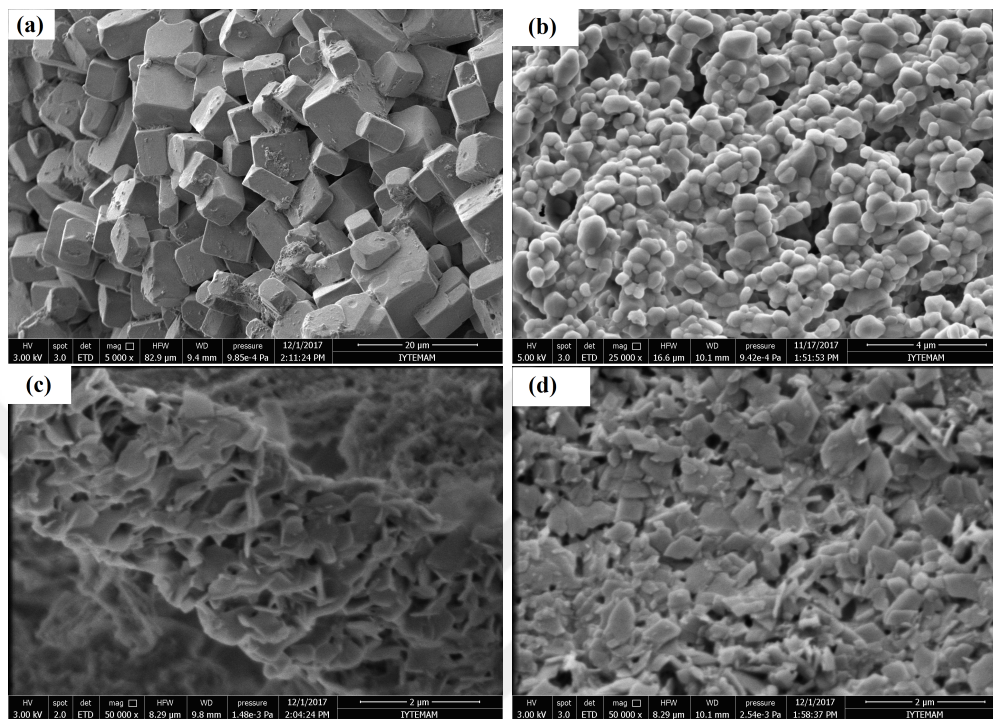
Figure 4.16: SEM images of freeze dried MIC at a concentration of 0.1 mg/mL and 1.0 mg/mL in PBS and water. (a) 0.1 mg/mL in PBS, (b) 1.0 mg/mL in PBS, (c) 0.1 mg/mL in water, and (d) 1.0 mg/mL in water.

4.6 Measurement of histotripsy threshold in agarose tissue phantoms using inclusion complex

In a previous study, it was reported that to generate the cavitation in a different tissues and tissue-mimicking mediums, the threshold of 26-30 MPa peak negative pressure was required [118]. When the pressure was increased above 26 MPa, cavitation occurred due to existing gas pockets in the tissue. When this bubble cavity fractionates, the cells adjacent to the bubble disrupts and forms a complete cavity, removing the tissue and forming a liquefied homogenate [20]. In order to see the effect of MIC in lowering down the threshold pressure, the pressure threshold was tested in the tissue-mimicking agarose phantoms with MIC, PFH and without the addition of material.

After carrying out the experiment, the results of the high-speed camera were observed and it was seen that in the first experiment, using the 500 kHz transducer, at lower driving voltage of 30 V, the MIC caused cavitation. At a driving voltage of 40 V, higher number of cavitation sites were observed in both the positive control and the tissue containing MIC. The phantom containing PFH also caused cavitation as it was the positive control, but the phantom without the addition of particle showed no cavitation. Figure 4.17 shows an image from the high-speed camera at threshold pressure of 30 V and 40 V, where it can be clearly seen that there is no cavitation in the agarose gel, whereas clear cavitation can be seen due to the MIC and PFH.
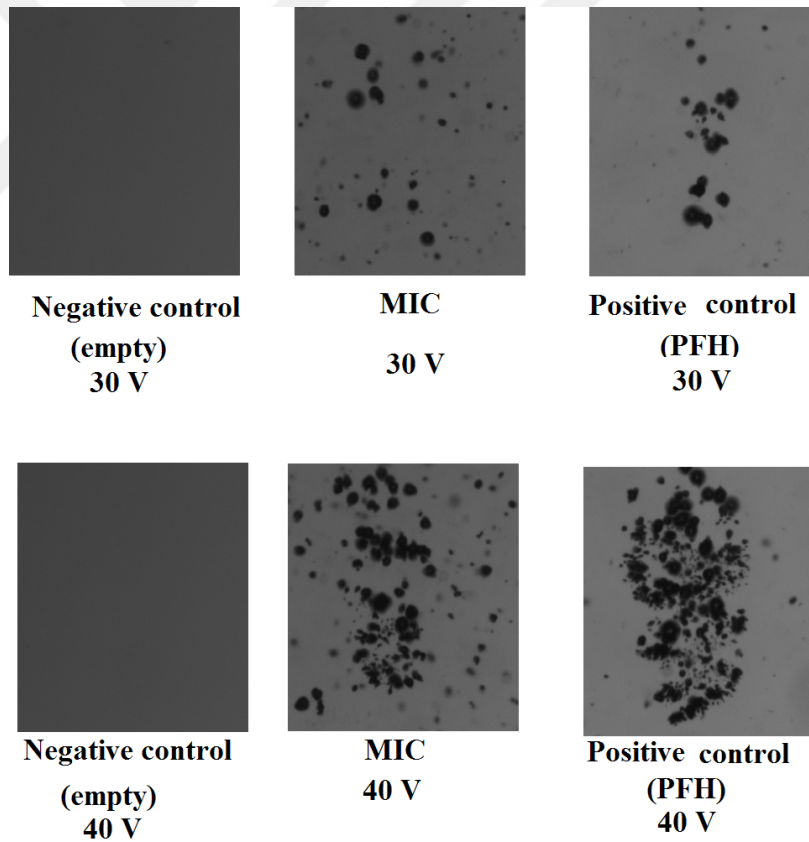
Figure 4.17: Bubble cloud was generated using MIC as historipsy agent in the agarose phantom.

Also, the same experiment was performed using the 700 kHz probe with 5 cycles per pulse. Voltages of 100 V and 150 V were used. The voltage at 150 V corresponds to the maximum pressure required for the histotripsy without any agent, where as 100 V corresponds to pressures lower than that. In Figure 4.18 It was clearly seen that at 100 V, the MIC was able to produce a bubble cloud, where as in the control nothing was present. Hence, concluding that the MIC were working properly for histotripsy.
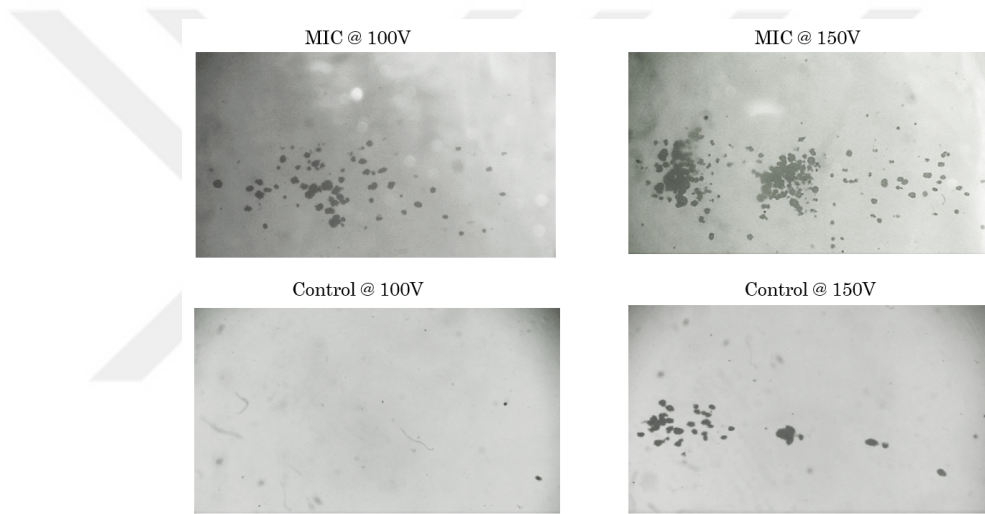
Figure 4.18: Bubble cloud was generated using MIC as historipsy agent in the agarose phantom at voltages of 100 V and 150 V using a 700 kHz transducer with 5 cycles per pulse.

Chapter 5

Conclusion

The goal of the study was to synthesize a new, easy to produce, and a cost-effective histotripsy agent which would perform as efficiently as the nanodroplets for the NMH. The obtained results support our hypothesis of formation of the inclusion complex using BCD/PFH and MCD/PFH. Additionally, the results show that MIC was superior to IC with regards to EE. Although further research is required, it can be hypothesized that more than one PFH can be encapsulated in the cavity of MCD.

Another outcome of the study was that the complete characterization of the MIC was performed. TGA gave critical data about its stability and degradation, and showed that it is stable at room temperature. Furthermore, DLS revealed that the MIC particles are small enough to be used in vivo, and that they have the potential to adapt the ERP effect. Hemolysis and cell toxicity studies proved that the MIC is non-toxic towards RBCs and kidney cells and hence can be used in vivo. Finally, the main goal of the study was achieved as the histotripsy experiment reported that MIC lowers the threshold pressure significantly.

Further research needs to be performed on different concentrations of MIC using focused US histotripsy and see the difference of cavitation bubbles under different concentrations. Computational models and simulations will also be a

part of the future experiments which will reveal the possible organizations of the host-guest chemistry and how they interact under different conditions. We will also perform the cell uptake experiments for MIC and see how they interact with cells once the MIC enters the cell membranes. For now, it can be concluded that the synthesized MIC is economical, simple to produce, commercializable, small, non-toxic, and successful in lowering the threshold cavitation pressure just as the nanodroplets.

Bibliography

[1] R. Siegel, D. Naishadham, and A. Jemal, "Cancer statistics, 2013," *CA: a cancer journal for clinicians*, vol. 63, no. 1, pp. 11–30, 2013.

[2] R. L. Siegel, K. D. Miller, S. A. Fedewa, D. J. Ahnen, R. G. Meester, A. Barzi, and A. Jemal, "Colorectal cancer statistics, 2017," *CA: a cancer journal for clinicians*, vol. 67, no. 3, pp. 177–193, 2017.

[3] R. L. Siegel, K. D. Miller, and A. Jemal, "Cancer statistics, 2016," *CA: a cancer journal for clinicians*, vol. 66, no. 1, pp. 7–30, 2016.

[4] Q. T. Ostrom, H. Gittleman, P. M. de Blank, J. L. Finlay, J. G. Gurney, R. McKean-Cowdin, D. S. Stearns, J. E. Wolff, M. Liu, Y. Wolinsky, *et al.*, "American brain tumor association adolescent and young adult primary brain and central nervous system tumors diagnosed in the united states in 2008-2012," *Neuro-oncology*, vol. 18, no. suppl_1, pp. i1–i50, 2015.

[5] J. Slots and T. E. Rams, "Antibiotics in periodontal therapy: advantages and disadvantages," *Journal of clinical periodontology*, vol. 17, no. s1, pp. 479–493, 1990.

[6] A. Pilar, M. Gupta, S. G. Laskar, and S. Laskar, "Intraoperative radiotherapy: review of techniques and results," *ecancermedicalscience*, vol. 11, 2017.

[7] S. A. Rosenberg, J. C. Yang, and N. P. Restifo, "Cancer immunotherapy: moving beyond current vaccines," *Nature medicine*, vol. 10, no. 9, pp. 909–915, 2004.

[8] S. M. Janib, A. S. Moses, and J. A. MacKay, "Imaging and drug delivery using theranostic nanoparticles," *Advanced drug delivery reviews*, vol. 62, no. 11, pp. 1052–1063, 2010.

[9] K.-y. Ng and Y. Liu, "Therapeutic ultrasound: its application in drug delivery," *Medicinal research reviews*, vol. 22, no. 2, pp. 204–223, 2002.

[10] M. A. Shampo and R. A. Kyle, "Karl theodore dussik?pioneer in ultrasound," in *Mayo Clinic Proceedings*, vol. 70, p. 1136, Elsevier, 1995.

[11] F. W. Kremkau, J. S. Kaufmann, M. M. Walker, P. G. Burch, and C. L. Spurr, "Ultrasonic enhancement of nitrogen mustard cytotoxicity in mouse leukemia," *Cancer*, vol. 37, no. 4, pp. 1643–1647, 1976.

[12] K. Tachibana, T. Uchida, K. Tamura, H. Eguchi, N. Yamashita, and K. Ogawa, "Enhanced cytotoxic effect of ara-c by low intensity ultrasound to hl-60 cells," *Cancer letters*, vol. 149, no. 1, pp. 189–194, 2000.

[13] K. Detre, R. Holubkov, S. Kelsey, M. Cowley, K. Kent, D. Williams, R. Myler, D. Faxon, D. Holmes Jr, M. Bourassa, *et al.*, "Percutaneous transluminal coronary angioplasty in 1985–1986 and 1977–1981," *New England Journal of Medicine*, vol. 318, no. 5, pp. 265–270, 1988.

[14] K. Ferrara, R. Pollard, and M. Borden, "Ultrasound microbubble contrast agents: fundamentals and application to gene and drug delivery," *Annual review of biomedical engineering*, vol. 9, 2007.

[15] S. Acharya and S. K. Sahoo, "Plga nanoparticles containing various anticancer agents and tumour delivery by epr effect," *Advanced drug delivery reviews*, vol. 63, no. 3, pp. 170–183, 2011.

[16] H. K. Makadia and S. J. Siegel, "Poly lactic-co-glycolic acid (plga) as biodegradable controlled drug delivery carrier," *Polymers*, vol. 3, no. 3, pp. 1377–1397, 2011.

[17] T. Boissenot, A. Bordat, E. Fattal, and N. Tsapis, "Ultrasound-triggered drug delivery for cancer treatment using drug delivery systems: From theoretical considerations to practical applications," *Journal of Controlled Release*, vol. 241, pp. 144–163, 2016.

[18] A.-L. Papa, N. Korin, M. Kanapathipillai, A. Mammoto, T. Mammoto, A. Jiang, R. Mannix, O. Uzun, C. Johnson, D. Bhatta, *et al.*, "Ultrasound-sensitive nanoparticle aggregates for targeted drug delivery," *Biomaterials*, 2017.

[19] Y. Yuksel Durmaz, E. Vlaisavljevich, Z. Xu, and M. ElSayed, "Development of nanodroplets for histotripsy-mediated cell ablation," *Molecular pharmaceutics*, vol. 11, no. 10, pp. 3684–3695, 2014.

[20] E. Vlaisavljevich, Y. Y. Durmaz, A. Maxwell, M. ElSayed, and Z. Xu, "Nanodroplet-mediated histotripsy for image-guided targeted ultrasound cell ablation," *Theranostics*, vol. 3, no. 11, p. 851, 2013.

[21] J. Owen, Q. Pankhurst, and E. Stride, "Magnetic targeting and ultrasound mediated drug delivery: benefits, limitations and combination," *International Journal of Hyperthermia*, vol. 28, no. 4, pp. 362–373, 2012.

[22] N. C. Nanda, "History of echocardiographic contrast agents," *Clinical cardiology*, vol. 20, no. S1, pp. 7–11, 1997.

[23] C. J. Harvey, J. M. Pilcher, R. J. Eckersley, M. J. Blomley, and D. O. Cosgrove, "Advances in ultrasound," *Clinical radiology*, vol. 57, no. 3, pp. 157–177, 2002.

[24] A. L. Klibanov, "Ligand-carrying gas-filled microbubbles: ultrasound contrast agents for targeted molecular imaging," *Bioconjugate chemistry*, vol. 16, no. 1, pp. 9–17, 2005.

[25] E. Quaia, *Contrast media in ultrasonography: basic principles and clinical applications.* Springer, 2006.

[26] S. Qin, C. F. Caskey, and K. W. Ferrara, "Ultrasound contrast microbubbles in imaging and therapy: physical principles and engineering," *Physics in medicine and biology*, vol. 54, no. 6, p. R27, 2009.

[27] D. L. Miller, N. B. Smith, M. R. Bailey, G. J. Czarnota, K. Hynynen, and I. R. S. Makin, "Overview of therapeutic ultrasound applications and safety considerations," *Journal of Ultrasound in Medicine*, vol. 31, no. 4, pp. 623–634, 2012.

[28] K. Tachibana and S. Tachibana, "Albumin microbubble echo-contrast material as an enhancer for ultrasound accelerated thrombolysis," *Circulation*, vol. 92, no. 5, pp. 1148–1150, 1995.

[29] J. R. Lindner and S. Kaul, "Delivery of drugs with ultrasound," *Echocardiography*, vol. 18, no. 4, pp. 329–337, 2001.

[30] Y. Wu, E. C. Unger, T. P. McCREERY, R. H. Sweitzer, D. Shen, G. Wu, and M. D. Vielhauer, "Binding and lysing of blood clots using mrx-408," *Investigative radiology*, vol. 33, no. 12, pp. 880–885, 1998.

[31] P. Prentice, A. Cuschieri, K. Dholakia, M. Prausnitz, and P. Campbell, "Membrane disruption by optically controlled microbubble cavitation," *Nature physics*, vol. 1, no. 2, pp. 107–110, 2005.

[32] R. K. Schlicher, H. Radhakrishna, T. P. Tolentino, R. P. Apkarian, V. Zarnitsyn, and M. R. Prausnitz, "Mechanism of intracellular delivery by acoustic cavitation," *Ultrasound in medicine & biology*, vol. 32, no. 6, pp. 915–924, 2006.

[33] S. Madersbacher, M. Pedevilla, L. Vingers, M. Susani, and M. Marberger, "Effect of high-intensity focused ultrasound on human prostate cancer in vivo," *Cancer research*, vol. 55, no. 15, pp. 3346–3351, 1995.

[34] J. Chapelon, J. Margonari, F. Vernier, F. Gorry, R. Ecochard, and A. Gelet, "In vivo effects of high-intensity ultrasound on prostatic adenocarcinoma dunning r3327," *Cancer research*, vol. 52, no. 22, pp. 6353–6357, 1992.

[35] S.-Q. Cheng, X.-D. Zhou, Z.-Y. Tang, Y. Yu, H.-Z. Wang, S.-S. Bao, and D.-C. Qian, "High-intensity focused ultrasound in the treatment of experimental liver tumour," *Journal of cancer research and clinical oncology*, vol. 123, no. 4, pp. 219–223, 1997.

[36] S. Madersbacher, C. Kratzik, M. Susani, and M. Marberger, "Minimally invasive therapy of benign prostatic hyperplasia with focussed ultrasound," *Der Urologe. Ausg. A*, vol. 34, no. 2, pp. 98–104, 1995.

[37] E. C. Unger, T. P. McCreery, R. H. Sweitzer, V. E. Caldwell, and Y. Wu, "Acoustically active liposheres containing paclitaxel: a new therapeutic ultrasound contrast agent," *Investigative radiology*, vol. 33, no. 12, pp. 886–892, 1998.

[38] H. R. Guzman, D. X. Nguyen, S. Khan, and M. R. Prausnitz, "Ultrasound-mediated disruption of cell membranes. ii. heterogeneous effects on cells," *The Journal of the Acoustical Society of America*, vol. 110, no. 1, pp. 597–606, 2001.

[39] R. J. Price, D. M. Skyba, S. Kaul, and T. C. Skalak, "Delivery of colloidal particles and red blood cells to tissue through microvessel ruptures created by targeted microbubble destruction with ultrasound," *Circulation*, vol. 98, no. 13, pp. 1264–1267, 1998.

[40] I. Lentacker, B. Geers, J. Demeester, S. C. De Smedt, and N. N. Sanders, "Design and evaluation of doxorubicin-containing microbubbles for ultrasound-triggered doxorubicin delivery: cytotoxicity and mechanisms involved," *Molecular Therapy*, vol. 18, no. 1, pp. 101–108, 2010.

[41] J. Xie, S. Lee, and X. Chen, "Nanoparticle-based theranostic agents," *Advanced drug delivery reviews*, vol. 62, no. 11, pp. 1064–1079, 2010.

[42] F. Yang, Y. Li, Z. Chen, Y. Zhang, J. Wu, and N. Gu, "Superparamagnetic iron oxide nanoparticle-embedded encapsulated microbubbles as dual contrast agents of magnetic resonance and ultrasound imaging," *Biomaterials*, vol. 30, no. 23, pp. 3882–3890, 2009.

[43] J. R. Hwu, Y. S. Lin, T. Josephrajan, M.-H. Hsu, F.-Y. Cheng, C.-S. Yeh, W.-C. Su, and D.-B. Shieh, "Targeted paclitaxel by conjugation to iron oxide and gold nanoparticles," *Journal of the American Chemical Society*, vol. 131, no. 1, pp. 66–68, 2008.

[44] T. K. Jain, M. A. Morales, S. K. Sahoo, D. L. Leslie-Pelecky, and V. Labhasetwar, "Iron oxide nanoparticles for sustained delivery of anticancer agents," *Molecular pharmaceutics*, vol. 2, no. 3, pp. 194–205, 2005.

[45] H. J. Kim, J. F. Greenleaf, R. R. Kinnick, J. T. Bronk, and M. E. Bolander, "Ultrasound-mediated transfection of mammalian cells," *Human gene therapy*, vol. 7, no. 11, pp. 1339–1346, 1996.

[46] A. Lawrie, A. Brisken, S. Francis, D. Cumberland, D. Crossman, and C. Newman, "Microbubble-enhanced ultrasound for vascular gene delivery," *Gene therapy*, vol. 7, no. 23, p. 2023, 2000.

[47] T. Li, K. Tachibana, M. Kuroki, and M. Kuroki, "Gene transfer with echo-enhanced contrast agents: comparison between albunex, optison, and levovist in mice?initial results," *Radiology*, vol. 229, no. 2, pp. 423–428, 2003.

[48] W. J. Greenleaf, M. E. Bolander, G. Sarkar, M. B. Goldring, and J. F. Greenleaf, "Artificial cavitation nuclei significantly enhance acoustically induced cell transfection," *Ultrasound in medicine & biology*, vol. 24, no. 4, pp. 587–595, 1998.

[49] A. Rahim, S. L. Taylor, N. L. Bush, G. R. Ter Haar, J. C. Bamber, and C. D. Porter, "Physical parameters affecting ultrasound/microbubble-mediated gene delivery efficiency in vitro," *Ultrasound in medicine & biology*, vol. 32, no. 8, pp. 1269–1279, 2006.

[50] E. C. Unger, E. Hersh, M. Vannan, T. O. Matsunaga, and T. McCreery, "Local drug and gene delivery through microbubbles," *Progress in cardiovascular diseases*, vol. 44, no. 1, pp. 45–54, 2001.

[51] R. V. Shohet, S. Chen, Y.-T. Zhou, Z. Wang, R. S. Meidell, R. H. Unger, and P. A. Grayburn, "Echocardiographic destruction of albumin microbubbles directs gene delivery to the myocardium," *Circulation*, vol. 101, no. 22, pp. 2554–2556, 2000.

[52] S. Tsunoda, O. Mazda, Y. Oda, Y. Iida, S. Akabame, T. Kishida, M. Shin-Ya, H. Asada, S. Gojo, J. Imanishi, *et al.*, "Sonoporation using microbubble br14 promotes pdna/sirna transduction to murine heart," *Biochemical and biophysical research communications*, vol. 336, no. 1, pp. 118–127, 2005.

[53] T. Kodama, A. Aoi, Y. Watanabe, S. Horie, M. Kodama, L. Li, R. Chen, N. Teramoto, H. Morikawa, S. Mori, *et al.*, "Evaluation of transfection efficiency in skeletal muscle using nano/microbubbles and ultrasound," *Ultrasound in medicine & biology*, vol. 36, no. 7, pp. 1196–1205, 2010.

[54] R. J. van den Bijgaart, D. C. Eikelenboom, M. Hoogenboom, J. J. Fütterer, M. H. den Brok, and G. J. Adema, "Thermal and mechanical high-intensity focused ultrasound: perspectives on tumor ablation, immune effects and combination strategies," *Cancer Immunology, Immunotherapy*, vol. 66, no. 2, pp. 247–258, 2017.

[55] G. D. Dodd, M. C. Soulen, R. A. Kane, T. Livraghi, W. R. Lees, Y. Yamashita, A. R. Gillams, O. I. Karahan, and H. Rhim, "Minimally invasive treatment of malignant hepatic tumors: at the threshold of a major breakthrough," *Radiographics*, vol. 20, no. 1, pp. 9–27, 2000.

[56] M. Zhu, X.-A. Lin, X.-M. Zha, W.-B. Zhou, T.-S. Xia, and S. Wang, "Evaluation of the therapeutic efficacy of sequential therapy involving percutaneous microwave ablation in combination with 131i-hypericin using the vx2 rabbit breast solid tumor model," *PloS one*, vol. 10, no. 3, p. e0120303, 2015.

[57] H. Webb, M. G. Lubner, and J. L. Hinshaw, "Thermal ablation," in *Seminars in roentgenology*, vol. 46, pp. 133–141, Elsevier, 2011.

[58] M. H. den Brok, R. P. Sutmuller, R. van der Voort, E. J. Bennink, C. G. Figdor, T. J. Ruers, and G. J. Adema, "In situ tumor ablation creates an

antigen source for the generation of antitumor immunity," *Cancer research*, vol. 64, no. 11, pp. 4024–4029, 2004.

[59] K. M. Prise and J. M. O'sullivan, "Radiation-induced bystander signalling in cancer therapy," *Nature Reviews Cancer*, vol. 9, no. 5, pp. 351–360, 2009.

[60] C. L. Brace, "Radiofrequency and microwave ablation of the liver, lung, kidney, and bone: what are the differences?," *Current problems in diagnostic radiology*, vol. 38, no. 3, pp. 135–143, 2009.

[61] R. Loffroy, L. Estivalet, S. Favelier, P. Pottecher, P.-Y. Genson, J. Cercueli, and D. Krausé, "Interventional radiology therapies for liver cancer," *Hepatoma Res*, vol. 2, pp. 1–9, 2016.

[62] M. Ahmed, C. L. Brace, F. T. Lee Jr, and S. N. Goldberg, "Principles of and advances in percutaneous ablation," *Radiology*, vol. 258, no. 2, pp. 351–369, 2011.

[63] Y. R. Huo and G. D. Eslick, "Microwave ablation compared to radiofrequency ablation for hepatic lesions: a meta-analysis," *Journal of Vascular and Interventional Radiology*, vol. 26, no. 8, pp. 1139–1146, 2015.

[64] A. Stang, R. Fischbach, W. Teichmann, C. Bokemeyer, and D. Braumann, "A systematic review on the clinical benefit and role of radiofrequency ablation as treatment of colorectal liver metastases," *European Journal of Cancer*, vol. 45, no. 10, pp. 1748–1756, 2009.

[65] G. Foltz, "Image-guided percutaneous ablation of hepatic malignancies," in *Seminars in interventional radiology*, vol. 31, pp. 180–186, Thieme Medical Publishers, 2014.

[66] S. Sartori, F. Di Vece, F. Ermili, and P. Tombesi, "Laser ablation of liver tumors: An ancillary technique, or an alternative to radiofrequency and microwave?," *World journal of radiology*, vol. 9, no. 3, p. 91, 2017.

[67] P. Tombesi, F. Di Vece, S. Sartori, *et al.*, "Radiofrequency, microwave, and laser ablation of liver tumors: time to move toward a tailored ablation technique," *Hepatoma Res*, vol. 1, no. 2, pp. 52–57, 2015.

[68] T. J. Vogl, P. Farshid, N. N. Naguib, A. Darvishi, B. Bazrafshan, E. Mbalisike, T. Burkhard, and S. Zangos, "Thermal ablation of liver metastases from colorectal cancer: radiofrequency, microwave and laser ablation therapies," *La radiologia medica*, vol. 119, no. 7, pp. 451–461, 2014.

[69] G. Francica, A. Petrolati, E. Di Stasio, S. Pacella, R. Stasi, and C. M. Pacella, "Effectiveness, safety, and local progression after percutaneous laser ablation for hepatocellular carcinoma nodules up to 4 cm are not affected by tumor location," *American Journal of Roentgenology*, vol. 199, no. 6, pp. 1393–1401, 2012.

[70] G. G. Di Costanzo, G. Francica, and C. M. Pacella, "Laser ablation for small hepatocellular carcinoma: State of the art and future perspectives," *World journal of hepatology*, vol. 6, no. 10, p. 704, 2014.

[71] L. C. Bertot, M. Sato, R. Tateishi, H. Yoshida, and K. Koike, "Mortality and complication rates of percutaneous ablative techniques for the treatment of liver tumors: a systematic review," *European radiology*, vol. 21, no. 12, pp. 2584–2596, 2011.

[72] P. T. Pepple and D. A. Gerber, "Laparoscopic-assisted ablation of hepatic tumors: a review," in *Seminars in interventional radiology*, vol. 31, pp. 125–128, Thieme Medical Publishers, 2014.

[73] J. E. Kennedy, "High-intensity focused ultrasound in the treatment of solid tumours," *Nature reviews cancer*, vol. 5, no. 4, pp. 321–327, 2005.

[74] T. Mason, "A sound investment," *Chemistry and Industry*, no. 21, pp. 878–82, 1998.

[75] A. Copelan, J. Hartman, M. Chehab, and A. M. Venkatesan, "High-intensity focused ultrasound: current status for image-guided therapy," in *Seminars in interventional radiology*, vol. 32, pp. 398–415, Thieme Medical Publishers, 2015.

[76] E. Vlaisavljevich, O. Aydin, Y. Y. Durmaz, K.-W. Lin, B. Fowlkes, Z. Xu, and M. E. ElSayed, "Effects of droplet composition on nanodroplet-mediated histotripsy," *Ultrasound in medicine & biology*, vol. 42, no. 4, pp. 931–946, 2016.

[77] E. Vlaisavljevich, K.-W. Lin, A. Maxwell, M. T. Warnez, L. Mancia, R. Singh, A. J. Putnam, B. Fowlkes, E. Johnsen, C. Cain, *et al.*, "Effects of ultrasound frequency and tissue stiffness on the histotripsy intrinsic threshold for cavitation," *Ultrasound in medicine & biology*, vol. 41, no. 6, pp. 1651–1667, 2015.

[78] Z. Xu, A. Ludomirsky, L. Y. Eun, T. L. Hall, B. C. Tran, J. B. Fowlkes, and C. A. Cain, "Controlled ultrasound tissue erosion," *IEEE transactions on ultrasonics, ferroelectrics, and frequency control*, vol. 51, no. 6, pp. 726–736, 2004.

[79] J.-M. Lehn, "Supramolecular chemistry?scope and perspectives molecules, supermolecules, and molecular devices (nobel lecture)," *Angewandte Chemie International Edition*, vol. 27, no. 1, pp. 89–112, 1988.

[80] K. Ariga and T. Kunitake, *Supramolecular chemistry-fundamentals and applications: advanced textbook*. Springer Science & Business Media, 2006.

[81] F. Wang, J. Zhang, X. Ding, S. Dong, M. Liu, B. Zheng, S. Li, L. Wu, Y. Yu, H. W. Gibson, *et al.*, "Metal coordination mediated reversible conversion between linear and cross-linked supramolecular polymers," *Angewandte Chemie*, vol. 122, no. 6, pp. 1108–1112, 2010.

[82] Z. Zhang, Y. Luo, J. Chen, S. Dong, Y. Yu, Z. Ma, and F. Huang, "Formation of linear supramolecular polymers that is driven by c? h??? π interactions in solution and in the solid state," *Angewandte Chemie*, vol. 123, no. 6, pp. 1433–1437, 2011.

[83] F. Wang, C. Han, C. He, Q. Zhou, J. Zhang, C. Wang, N. Li, and F. Huang, "Self-sorting organization of two heteroditopic monomers to supramolecular alternating copolymers," *Journal of the American Chemical Society*, vol. 130, no. 34, pp. 11254–11255, 2008.

[84] J. Jing, A. Szarpak-Jankowska, R. Guillot, I. Pignot-Paintrand, C. Picart, and R. Auze?ly-Velty, "Cyclodextrin/paclitaxel complex in biodegradable capsules for breast cancer treatment," *Chemistry of Materials*, vol. 25, no. 19, pp. 3867–3873, 2013.

[85] N. J. Wheate, D. P. Buck, A. I. Day, and J. G. Collins, "Cucurbit [n] uril binding of platinum anticancer complexes," *Dalton transactions*, no. 3, pp. 451–458, 2006.

[86] Y. Zhao, D. P. Buck, D. L. Morris, M. H. Pourgholami, A. I. Day, and J. G. Collins, "Solubilisation and cytotoxicity of albendazole encapsulated in cucurbit [n] uril," *Organic & biomolecular chemistry*, vol. 6, no. 24, pp. 4509–4515, 2008.

[87] S. K. Menon, N. R. Modi, B. Mistry, and K. Joshi, "Improvement of some pharmaceutical properties of mycophenolate mofetil (mmf) by para sulphonatocalix [4] resorcinarene inclusion complex," *Journal of Inclusion Phenomena and Macrocyclic Chemistry*, vol. 70, no. 1-2, pp. 121–128, 2011.

[88] M. B. Patel, N. N. Valand, N. R. Modi, K. V. Joshi, U. Harikrishnan, S. P. Kumar, Y. T. Jasrai, and S. K. Menon, "Effect of p-sulfonatocalix [4] resorcinarene (psc [4] r) on the solubility and bioavailability of a poorly water soluble drug lamotrigine (lmn) and computational investigation," *RSC Advances*, vol. 3, no. 36, pp. 15971–15981, 2013.

[89] S. K. Menon, B. R. Mistry, K. V. Joshi, N. R. Modi, and D. Shashtri, "Evaluation and solubility improvement of carvedilol: Psc [n] arene inclusion complexes with acute oral toxicity studies," *Journal of Inclusion Phenomena and Macrocyclic Chemistry*, vol. 73, no. 1-4, pp. 295–303, 2012.

[90] Z. Xu, J. B. Fowlkes, and C. A. Cain, "A new strategy to enhance cavitational tissue erosion using a high-intensity, initiating sequence," *IEEE transactions on ultrasonics, ferroelectrics, and frequency control*, vol. 53, no. 8, pp. 1412–1424, 2006.

[91] G. Tiwari, R. Tiwari, and A. K. Rai, "Cyclodextrins in delivery systems: Applications," *Journal of Pharmacy and Bioallied Sciences*, vol. 2, no. 2, p. 72, 2010.

[92] S. Menuel, J.-P. Joly, B. Courcot, J. Elysée, N.-E. Ghermani, and A. Marsura, "Synthesis and inclusion ability of a bis-β-cyclodextrin pseudo-cryptand towards busulfan anticancer agent," *Tetrahedron*, vol. 63, no. 7, pp. 1706–1714, 2007.

[93] M. E. Davis and M. E. Brewster, "Cyclodextrin-based pharmaceutics: past, present and future," *Nature Reviews Drug Discovery*, vol. 3, no. 12, pp. 1023–1035, 2004.

[94] V. Gold, K. Loening, A. McNaught, and P. Shemi, "Iupac compendium of chemical terminology," *Blackwell Science, Oxford*, 1997.

[95] D. M. Lemal, "Perspective on fluorocarbon chemistry," *The Journal of organic chemistry*, vol. 69, no. 1, pp. 1–11, 2004.

[96] R. Díaz-López, N. Tsapis, and E. Fattal, "Liquid perfluorocarbons as contrast agents for ultrasonography and 19f-mri," *Pharmaceutical research*, vol. 27, no. 1, p. 1, 2010.

[97] M. Ragaller, J. Bleyl, T. Koch, and D. Albrecht, "From isoflurane to perfluorohexane? perfluorocarbons–therapeutic strategies in acute lung failure," *Der Anaesthesist*, vol. 49, no. 4, pp. 291–301, 2000.

[98] M. Schneider, M. Arditi, M.-b. Barrau, J. Brochot, A. Broillet, R. Ventrone, and F. Yan, "Br1: a new ultrasonographic contrast agent based on sulfur hexafluoride-filled microbubbles.," *Investigative radiology*, vol. 30, no. 8, pp. 451–457, 1995.

[99] J. U. Bleyl, M. Ragaller, U. Tschö, M. Regner, M. Hübler, M. Kanzow, O. Vincent, and M. Albrecht, "Changes in pulmonary function and oxygenation during application of perfluorocarbon vapor in healthy and oleic acid-injured animals," *Critical care medicine*, vol. 30, no. 6, pp. 1340–1347, 2002.

[100] M. G. de Abreu, A. D. Quelhas, P. Spieth, G. Bräuer, L. Knels, M. Kasper, A. V. Pino, J.-U. Bleyl, M. Hübler, F. Bozza, *et al.*, "Comparative effects of vaporized perfluorohexane and partial liquid ventilation in oleic acid–induced lung injury," *The Journal of the American Society of Anesthesiologists*, vol. 104, no. 2, pp. 278–289, 2006.

[101] S. B. Feinstein, "Contrast agents for ultrasonic imaging," Jan. 12 1988. US Patent 4,718,433.

[102] S. C. Quay, "Ultrasound contrast media comprising perfluoropentane and perfluorohexane gas," Sept. 24 1996. US Patent 5,558,854.

[103] Y. Gan, Y. Zhang, C. Xiao, C. Zhou, and Y. Zhao, "A novel preparation of methyl-β-cyclodextrin from dimethyl carbonate and β-cyclodextrin," *Carbohydrate research*, vol. 346, no. 3, pp. 389–392, 2011.

[104] N. Alkayal, G. Zapsas, P. Bilalis, and N. Hadjichristidis, "Self-assembly behavior of well-defined polymethylene-block-poly (ethylene glycol) copolymers in aqueous solution," *Polymer*, vol. 107, pp. 415–421, 2016.

[105] E. Damiani, R. Tursilli, A. Casolari, P. Astolfi, L. Greci, and S. Scalia, "Effect of complexation with randomly methylated β-cyclodextrin on the aqueous solubility, photostability and antioxidant activity of an indolinonic nitroxide radical," *Free radical research*, vol. 39, no. 1, pp. 41–49, 2005.

[106] S. Agatonovic-Kustrin, B. Glass, M. Brown, and M. Lebete, "For and against the use of methylated cyclodextrins in the development of midazolam solution for nasal application," *Austin J Pharmacol Ther*, vol. 2, no. 2, p. 3, 2014.

[107] L. M. Pinto, L. F. Fraceto, M. H. A. Santana, T. A. Pertinhez, S. O. Junior, and E. de Paula, "Physico-chemical characterization of benzocaine-β-cyclodextrin inclusion complexes," *Journal of pharmaceutical and biomedical analysis*, vol. 39, no. 5, pp. 956–963, 2005.

[108] W. Guo, B. Fung, and S. Christian, "Nmr study of cyclodextrin inclusion of fluorocarbon surfactants in solution," *Langmuir*, vol. 8, no. 2, pp. 446–451, 1992.

[109] H. Rachmawati, C. A. Edityaningrum, and R. Mauludin, "Molecular inclusion complex of curcumin–β-cyclodextrin nanoparticle to enhance curcumin skin permeability from hydrophilic matrix gel," *Aaps Pharmscitech*, vol. 14, no. 4, pp. 1303–1312, 2013.

[110] R. Moynihan, "The molecular structure of perfluorocarbon polymers. infrared studies on polytetrafluoroethylene1," *Journal of the American Chemical Society*, vol. 81, no. 5, pp. 1045–1050, 1959.

[111] S. Pawsey and L. Reven, "19f fast magic-angle spinning nmr studies of perfluoroalkanoic acid self-assembled monolayers," *Langmuir*, vol. 22, no. 3, pp. 1055–1062, 2006.

[112] H. Tatsuno and S. Ando, "Structure and dynamics of perfluoroalkane/β-cyclodextrin inclusion compounds as studied by solid-state 19f mas and 1h? 19f cp/mas nmr spectroscopy," *The Journal of Physical Chemistry B*, vol. 110, no. 51, pp. 25751–25760, 2006.

[113] A. H. Karoyo, A. S. Borisov, L. D. Wilson, and P. Hazendonk, "Formation of host-guest complexes of β-cyclodextrin and perfluorooctanoic acid," *The Journal of Physical Chemistry B*, vol. 115, no. 31, pp. 9511–9527, 2011.

[114] G. Zhu, Z. Xiao, R. Zhou, and Y. Zhu, "Study of production and pyrolysis characteristics of sweet orange flavor-β-cyclodextrin inclusion complex," *Carbohydrate polymers*, vol. 105, pp. 75–80, 2014.

[115] T. M. Allen and P. R. Cullis, "Drug delivery systems: entering the mainstream," *Science*, vol. 303, no. 5665, pp. 1818–1822, 2004.

[116] M. Yu, C. Zhou, L. Liu, S. Zhang, S. Sun, J. D. Hankins, X. Sun, and J. Zheng, "Interactions of renal-clearable gold nanoparticles with tumor microenvironments: Vasculature and acidity effects," *Angewandte Chemie*, vol. 129, no. 15, pp. 4378–4383, 2017.

[117] T. Mocan, "Hemolysis as expression of nanoparticles-induced cytotoxicity in red blood cells," *Biotechnol Mol Biol Nanomed*, vol. 1, no. 7, 2013.

[118] A. D. Maxwell, C. A. Cain, T. L. Hall, J. B. Fowlkes, and Z. Xu, "Probability of cavitation for single ultrasound pulses applied to tissues and tissue-mimicking materials," *Ultrasound in medicine & biology*, vol. 39, no. 3, pp. 449–465, 2013.

Appendix A

Appendix

DEVELOPMENT OF A HISTOTRIPSY AGENT USING HOST-GUEST INTERACTION